Goli *et al. Earth, Planets and Space* (2025) 77:167
https://doi.org/10.1186/s40623-025-02277-8

Earth, Planets and Space

FULL PAPER **Open Access**

Geoid determination using airborne gravity vectors

Mehdi Goli[1], Ismael Foroughi[2,5*], Spiros Pagiatakis[2], Stephen Ferguson[3] and Pavel Novák[4]

Abstract

In traditional airborne gravimetry, the vertical component of the gravity vector is used as an approximation of the measured magnitude of the gravity vector, which enters the determination of the local geoid. In this study, a comprehensive computational scheme for determining the local geoid using three components of the airborne gravity vector is presented. Our approach extends the existing one-step method for local geoid modeling by incorporating the full gravity vector measured by airborne sensors as boundary values in the gravimetric boundary-value problem. We derive integral kernel functions along with far-zone contributions for the three components of the airborne gravity vector and apply deterministic modifications to them. To validate our derivations, we use a global geopotential model (GGM)-based airborne gravity vectors burdened with realistic colored noise at one of the most challenging test sites for geoid determination, the 1-cm geoid test area in Colorado (USA). Results of closed-loop tests confirm that applying all three components of the GGM-based airborne gravity vector improves the internal accuracy of the geoid by 50% compared to using only the vertical component. We further use real airborne gravity vectors observed at a test site in the same region and show that the STD of the estimated geoid heights evaluated against the reference geoidal heights along the Geoid Slope Validation Survey of 2017 (GSVS17) Line is 2.3 cm using the "traditional approach" and 1.3 cm including the horizontal components. This indicates a significant improvement in the external accuracy (~ 46%) of the geoid when the full gravity vector is used, without using other heterogeneous observations.

Keywords One-step method, Gravity inversion, Geoid, Airborne gravimetry, Gravity vector

---

*Correspondence:
Ismael Foroughi
I.Foroughi@unb.ca
Full list of author information is available at the end of the article

Graphical Abstract

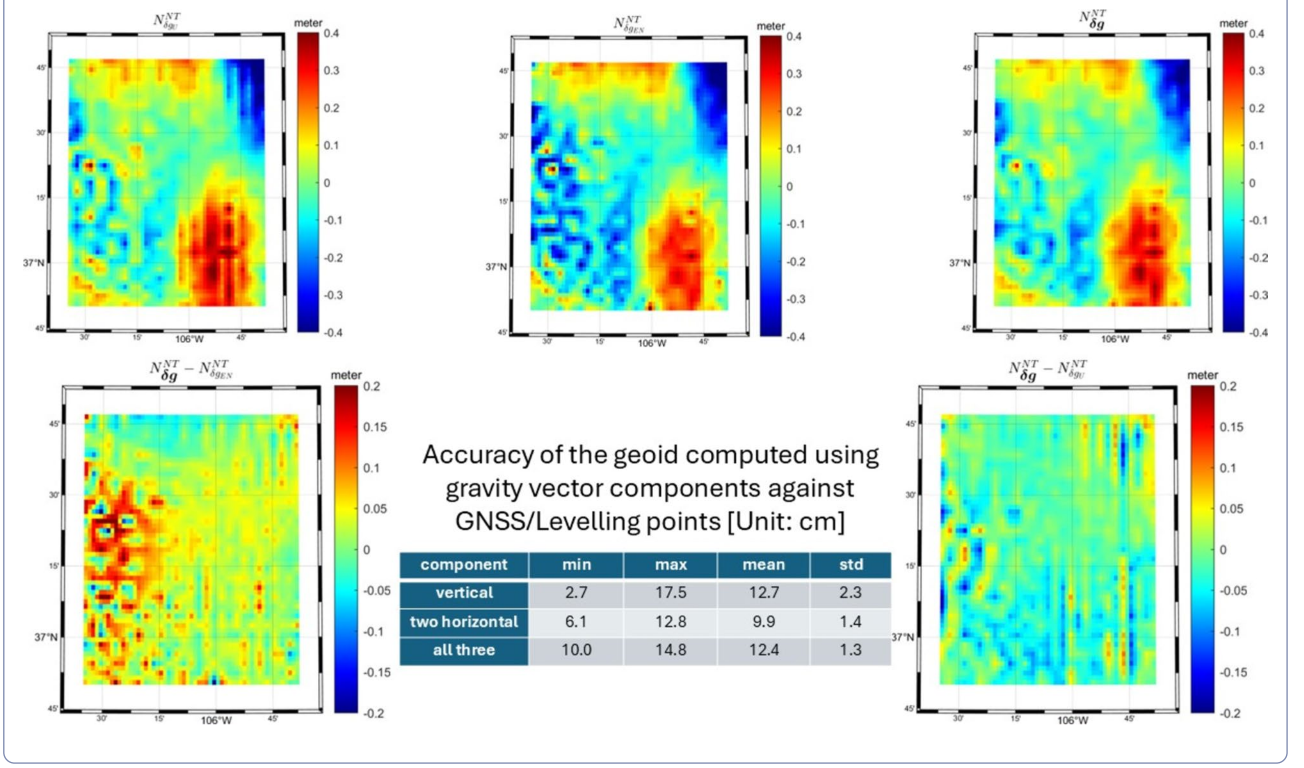

Accuracy of the geoid computed using gravity vector components against GNSS/Levelling points [Unit: cm]

component	min	max	mean	std
vertical	2.7	17.5	12.7	2.3
two horizontal	6.1	12.8	9.9	1.4
all three	10.0	14.8	12.4	1.3

1 Introduction

In geodesy, determining the geoid is one of the most important tasks as it concerns the shape of the Earth. The geoid is also a reference (zero-height) surface for physical heights that vertically position points on or above the Earth's surface considering physical (gravity) laws. Gravity data, vital for geoid determination under the continents, are collected by various sensors. It is usually classified as surface, airborne, and satellite gravity which is, respectively, derived from signals measured by static surface gravimeters and moving sensors on board of aircraft and satellites. Surface gravity has the advantage of being most accurate and covering the full spectrum, but surface data are discrete, irregularly distributed in space and regionally limited. Airborne data have the advantage of covering quickly and economically larger geographic areas avoiding various limitations related to their accessibility, but it is regionally, and due to the observation noise (needing to be filtered out), spectrally limited. Satellite data provide (almost) global coverage but are even more spectrally limited due to the attenuation of the gravitational field and the observation noise. Due to the geometry of satellite orbits, their spatial sampling has some deficiencies.

The low-frequency component of the geoidal height, usually derived from some suitable satellite-only global gravitational model (GGM), is regionally supplemented with the high-frequency component that is estimated using surface gravity. Airborne gravity can bridge the gap by mapping inaccessible areas, though it also lacks high frequencies due to the attenuation of the gravitational field with altitude and filtering of the measured signal to reduce its significant high-frequency noise despite using various stabilized platforms (Lacoste 1967; Swain 1996; Li 2011; Zhong et al. 2015; Becker 2016; Willberg et al. 2020; Bolotin et al. 2022; Golovan & Vyazmin 2023). Although various gravity data types are combined in practice to determine the regional geoid, this study is focused on using only spectrally limited airborne gravity data. The main contribution of this study is the formulation and testing of a comprehensive computational scheme for determining the local geoid model using all three components of the gravity vector measured by current airborne gravimeters.

Improved airborne gravimeters and signal processing techniques can now provide high-resolution gravity data with a wavelength of 1–1.5 km and an accuracy better than 1 mGal, provided the aircraft maintains steady flight at low altitudes (Argyle et al. 2000; Sander et al. 2011; Ferguson et al. 2017; Krasnov et al. 2022; Bidel et al. 2023; Foroughi et al. 2023; Vyazmin & Golovan 2023a). Such data have a positive impact on regional geoid modeling as it has been shown that densifying the coverage of gravity data can improve the accuracy of the gravimetric geoid model more than expanding their high-frequency content or reducing their observational noise (Ågren & Sjöberg 2014; Featherstone et al. 2018; Afrasteh et al. 2019; Goli et al. 2019b; Foroughi et al. 2019).

Airborne scalar gravity, approximating the vertical component of the gravity vector and interpolated into regular coordinate grids, has almost exclusively been utilized for determining local geoid models in geodesy. This "traditional approach", see, e.g., Schwarz & Li (1996) or Forsberg et al. (2000), has been considered, since horizontal components of the gravity vector were either not measured or their accuracy was poor (Schwarz et al. 2002). Improved stabilization of airborne gravimeters, three-axis inertial navigation systems, and accurate observations of aircraft velocity and acceleration vectors now allow the measurement of all three components of the gravity vector in a local (sensor-defined) Cartesian coordinate frame (Jekeli and Kwon 2002; Sander et al. 2005; Vyazmin et al. 2021; Vyazmin & Golovan 2023b).

There are only a few studies available that discuss the application of observed horizontal components of the airborne gravity vector to local geoid modeling. This is due to the low precision of gyroscopes and horizontal accelerometers in older gravimeter systems as well as limitations imposed by the stability of the aircraft (Serpas & Jekeli 2005). Feizi et al. (2021) employed airborne gravity vectors measured over Tanzania using local harmonic analysis methods and applied their horizontal components for local gravity field modeling. Vyazmin (2023) proposed a method to determine the gravity disturbance vector from airborne gravity derived using inertial and global satellite navigation systems and estimated a local gravity model using spherical scaling functions. Ferguson et al. (2017) used least-squares collocation to combine airborne vector gravity with surface scalar gravity in Western Australia. However, generally, these studies did not include geoid determination and focused more on gravity field modeling. Deng et al. (2020) applied horizontal components of the GGM-based airborne gravity vector for local geoid determination but did not use vertical component.

While the use of the Poisson integral equation for global geoid determination is established in the literature, e.g., in Novák et al. (2021), no study has provided a comprehensive scheme for computing the geoidal height involving all three components of the airborne gravity vector. Such a computational scheme must contain integral kernels and their modifications, far-zone contributions associated with horizontal components, and analyses of geoidal heights derived from scalar and vector gravity data. We address this gap by expanding the one-step method for geoid determination as proposed by Novák et al. (2003) for the vertical component of the gravity vector. Our computational scheme incorporates all three components of the airborne gravity vector, thus integrating the horizontal components into the computational scheme. The entire scheme is implemented and tested using GGM-based as well as real airborne gravity vectors. The contribution of the horizontal components to the estimated geoid and its accuracy is evaluated.

Methods, such as least-squares collocation, local harmonic expansions, and SRBF modeling (e.g., Chang et al. 2024), offer alternative frameworks for inverting airborne gravity data. However, these approaches often involve solving large normal equations or constructing global basis functions, which may pose computational challenges for high-resolution applications. In this study, we adopt a one-step integral formulation that results in a sparse design matrix and is well suited for efficient iterative solvers.

The one-step method for local geoid determination using scalar airborne gravity is briefly recapitulated and extended to the full gravity vector in Sect. 2. The strategy for solving numerically discretized integral equations is described in Sect. 3, followed by a discussion in Sect. 4. Results of numerical tests using both GGM-based and real airborne gravity vectors are presented in Sect. 5. A summary of the study and conclusions are presented in Sect. 6.

2 Theory

The upward continuation of the disturbing potential T in mass-free space from a sphere of radius R to a point in its exterior is solved by the spherical Poisson integral (Heiskanen and Moritz 1967, Ch. 1–16)

$$T(r,\Omega) = \frac{1}{4\pi}\int\limits_{\Omega_G} T\left(R,\Omega'\right)P(R,\psi,r)\mathrm{d}\Omega', \tag{1}$$

where Ω_G represents the full spatial angle, r denotes the geocentric radius of the external point (where data is measured), and $\Omega = (\varphi,\lambda)$ represents its spherical latitude and longitude. Angular coordinates of the integration point (where the unknown potential is solved) are denoted by $\Omega' = \left(\varphi',\lambda'\right)$ and the infinitesimal surface of a unit sphere is $\mathrm{d}\Omega' = \cos\varphi'\mathrm{d}\varphi'\mathrm{d}\lambda'$. The geocentric sphere of radius R approximates locally the unknown geoid. Finally, the spherical distance between the computation and integration points is denoted as ψ and P represents the unitless and isotropic spherical Poisson kernel function; see Eq. (2). In spherical approximation, $r = R + h$, where h is the height of the computation point. In the case of airborne gravimetry, observation points are positioned by global navigation satellite systems (GNSS) in a geocentric coordinate system. For given radius of the geocentric sphere, their heights can be computed. The gravity disturbance vector (GDV) at flight height is derived from the observed gravity vector by subtracting a normal gravity vector upward continued from the reference ellipsoid to the observation point.

To use Eq. (1) in practice, the disturbing potential T must be a harmonic function of 3D position everywhere outside the geoid. This is achieved by removing gravitational effects of all masses outside the geoid from the disturbing potential. Harmonization of the disturbing potential and GDVs outside the geoid is outlined in Sect. 4 but details are out of the scope of this study as they can be found in the literature (Vaníček et al. 1999, 2004; Vajda et al. 2020). Equation (1) represents the basis for formulating integral equations transforming GDVs measured by airborne sensors to the disturbing potential on the geoid. Novák et al. (2021) formulated integral equations that relate gradients of the disturbing potential outside the sphere to the disturbing potential on the sphere. In this study, we extend this theory and formulate the computational scheme (including kernel modifications and far-zone contributions) for airborne GDVs to determine the geoid using the one-step method.

2.1 Integral equations for horizontal components of GDVs

The spatial form of the Poisson function P in Eq. (1) is (Heiskanen and Moritz 1967, Ch. 1–16)

$$P(r,\psi,R) = \frac{R\left(r^2 - R^2\right)}{L^3(r,\psi,R)} - \frac{R}{r} - 3\left(\frac{R}{r}\right)^2 \cos\psi, \tag{2}$$

with the spatial distance L between the computation point (r,Ω) and the integration point $\left(R,\ \Omega'\right)$

$$L(r,\psi,R) = \sqrt{r^2 + R^2 - 2Rr\cos\psi}, \tag{3}$$

and cosine of their spherical distance

$$\cos\psi = \sin\varphi\sin\varphi' + \cos\varphi\cos\varphi'\cos\left(\lambda - \lambda'\right). \tag{4}$$

Note that the spherical Poisson function in Eq. (2) corresponds to the disturbing potential that does not include terms of degrees 0 and 1 in its spectral representation using a series of Legendre functions. GDV, denoted as $\delta\mathbf{g}$ (vectors and matrices are in the boldface font), is defined as the gradient of the disturbing potential. Using spherical coordinates and standard sign convention (gravitation attenuates with increasing elevation), $\delta\mathbf{g}$ reads (coordinates as parameters of functions are for brevity omitted)

$$\delta\mathbf{g} = \nabla T = \begin{bmatrix} \delta g_N \\ \delta g_E \\ \delta g_U \end{bmatrix} = \begin{bmatrix} \frac{1}{r}\frac{\partial T}{\partial\varphi} \\ \frac{1}{r\cos\varphi}\frac{\partial T}{\partial\lambda} \\ -\frac{\partial T}{\partial r} \end{bmatrix}, \tag{5}$$

where δg_E, δg_N, and δg_U represent, respectively, the east, north, and vertical (upward) components of GDV. The east and north components are collectively referred to as horizontal components. Substituting Eq. (5) to Eq. (1) and by applying the gradient operator on the spherical Poisson function at flight height, one obtains a vector-valued spherical Poisson integral equation (sought T is under the integral)

$$\delta\mathbf{g}(r,\Omega) = \frac{1}{4\pi R}\int_{\Omega_G} T\left(R,\Omega'\right)\mathbf{P}(r,\psi,R)\,\mathrm{d}\Omega', \tag{6}$$

with a vector-valued integral kernel function $\mathbf{P} = \left[P_N, P_E, P_U\right]^T$ defined as the gradient of the spherical Poisson function multiplied by radius R (to keep the kernel functions unitless), see Eq. (2). In spherical coordinates, it reads as follows (parameters of functions are again omitted):

$$\mathbf{P} = R\nabla P = \begin{bmatrix} P_N \\ P_E \\ P_U \end{bmatrix} = R\begin{bmatrix} \frac{1}{r}\frac{\partial P}{\partial\varphi} \\ \frac{1}{r\cos\varphi}\frac{\partial P}{\partial\lambda} \\ -\frac{\partial P}{\partial r} \end{bmatrix}. \tag{7}$$

Equation (6) represents an over-determined mathematical model (or observation equation) of the form of Fredholm's integral equation of the first kind. When solving it for the unknown disturbing potential T, two sub-problems are solved simultaneously: 1—measured airborne GDVs are continued down to the sphere approximating locally the geoid, and 2—they are transformed into the disturbing potential; hence the adjective "one-step" in the name of the method. Note that only the vertical component P_U of the vector-valued kernel function $\mathbf{P}$ is isotropic in the local reference frame as the horizontal components P_N and P_E depend also on the azimuth α between the computation and integration point.

By taking the negative radial derivative of the spherical Poisson function P, the unitless integral kernel P_U reads (zero- and first-degree terms in the spectral form of the function are again omitted)

$$P_U(r,\psi,R) = R^2\frac{3R^3\cos\psi - 5R^2 r + Rr^2\cos\psi + r^3}{L^5(r,\psi,R)} - \left(\frac{R}{r}\right)^2 - 6\left(\frac{R}{r}\right)^3\cos\psi. \tag{8}$$

Next, we adopt the one-step method also for the horizontal components of GDV. Using the chain rule of differentiation for $\frac{\partial P}{\partial\varphi}$ and $\frac{\partial P}{\partial\lambda}$, i.e., $\frac{\partial P}{\partial\varphi} = \frac{\partial P}{\partial\cos\psi}\frac{\partial\cos\psi}{\partial\varphi}$ and $\frac{\partial P}{\partial\lambda} = \frac{\partial P}{\partial\cos\psi}\frac{\partial\cos\psi}{\partial\lambda}$, and considering Eq. (4), horizontal components P_N and P_E of the vector-valued kernel function **P** read

$$\begin{bmatrix} P_N \\ P_E \end{bmatrix} = \frac{R}{r}\frac{\partial P}{\partial\cos\psi}\begin{bmatrix} \frac{\partial\cos\psi}{\partial\varphi} \\ \frac{1}{\cos\varphi}\frac{\partial\cos\psi}{\partial\lambda} \end{bmatrix}. \tag{9}$$

From Eq. (2) we obtain

$$\frac{R}{r}\frac{\partial P(r,\psi,R)}{\partial\cos\psi} = \frac{3R^3\left(r^2 - R^2\right)}{L^5(r,\psi,R)} - 3\left(\frac{R}{r}\right)^3. \tag{10}$$

Using the azimuth α between the computation and integration points, we can simplify Eq. (9) by setting (Heiskanen and Moritz 1967, Ch. 2–22)

$$\begin{bmatrix} \frac{\partial\cos\psi}{\partial\varphi} \\ \frac{1}{\cos\varphi}\frac{\partial\cos\psi}{\partial\lambda} \end{bmatrix} = \sin\psi\begin{bmatrix} \cos\alpha \\ \sin\alpha \end{bmatrix}, \tag{11}$$

and finally

$$\begin{bmatrix} P_N \\ P_E \end{bmatrix} = \frac{3R^3\left(r^2 - R^2\right)}{L^5(r,\psi,R)}\sin\psi\begin{bmatrix} \cos\alpha \\ \sin\alpha \end{bmatrix} - 3\left(\frac{R}{r}\right)^3\sin\psi\begin{bmatrix} \cos\alpha \\ \sin\alpha \end{bmatrix}. \tag{12}$$

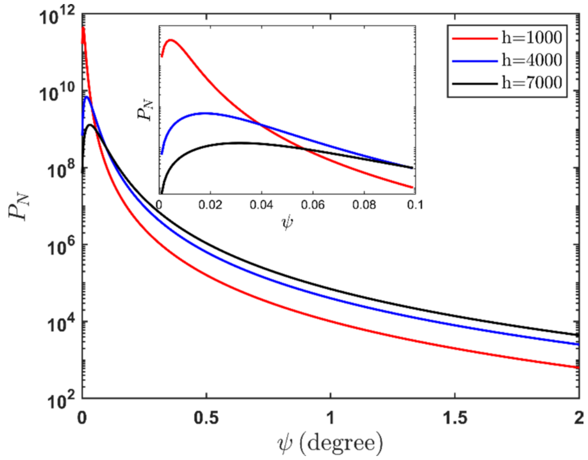

Fig. 1 North kernel component P_N (unitless) for $\alpha = 0, \psi \leq 2^\circ$ and three different heights h (m). The small box shows the behavior of the kernel component within the innermost zone $\psi \leq 0.1^\circ$

To understand how the horizontal kernel components P_N and P_E of the vector-valued kernel function **P** behave as functions of the spherical distance ψ, we plot values of the north kernel component P_N for the azimuth $\alpha = 0$ and three different observation heights h in Fig. 1. The north kernel component P_N (same applies for the east kernel component P_E and $\alpha = \pi/2$) has the largest magnitude close to the computation point. As the spherical distance ψ increases, the kernel components P_N and P_E attenuate rapidly. The plot of the spatial form of the vertical kernel component P_U can be found in Novák, (2003).

The spectral form of the spherical Poisson function reads (Heiskanen and Moritz 1967, Ch. 1–16)

$$P(r,\psi,R) = \sum_{n=2}^{\infty}\left(\frac{R}{r}\right)^{n+1}(2n+1)P_n(\cos\psi), \tag{13}$$

where P_n is the Legendre polynomial of degree n. The spectral form of the vertical kernel component can be obtained by differentiation of the series in Eq. (13) with respect to radius r (Novák, 2003), that is

$$P_U(r,\psi,R) = -R\frac{\partial P(r,\psi,R)}{\partial r} = \sum_{n=2}^{\infty}\left(\frac{R}{r}\right)^{n+2}(n+1)(2n+1)P_n(\cos\psi). \tag{14}$$

To maintain the unitless kernel, the radial derivative in Eq. (14) is multiplied by radius R (same scaling is applied below). The corresponding spectral form of the horizontal kernel components P_N and P_E can be derived by differentiating Eq. (13) with respect to the spherical coordinates φ and λ. Similarly to Eq. (11), one obtains

$$\begin{bmatrix} P_N \\ P_E \end{bmatrix} = \frac{R}{r}\frac{\partial P}{\partial\cos\psi}\sin\psi\begin{bmatrix} \cos\alpha \\ \sin\alpha \end{bmatrix}. \tag{15}$$

The derivative of the Poisson function can be represented using the spectral form in Eq. (13), that is

$$\frac{\partial P}{\partial\cos\psi} = \sum_{n=2}^{\infty}\left(\frac{R}{r}\right)^{n+1}(2n+1)\frac{\mathrm{d}P_n(\cos\psi)}{\mathrm{d}\cos\psi}. \tag{16}$$

The definition of the associated Legendre function $P_{n,1}(\cos\psi) = \sin\psi\frac{\mathrm{d}P_n(\cos\psi)}{\mathrm{d}\cos\psi}$ finally yields

$$\begin{bmatrix} P_N \\ P_E \end{bmatrix} = \begin{bmatrix} \cos\alpha \\ \sin\alpha \end{bmatrix}\sum_{n=2}^{\infty}\left(\frac{R}{r}\right)^{n+2}(2n+1)P_{n,1}(\cos\psi). \tag{17}$$

2.2 Remove–compute–restore approach

The low-frequency disturbing potential T_ℓ is estimated using GGM up to degree ℓ that reflects both the trust in the applied GGM and the geographic dimension of the area with measured airborne GDVs. The high-frequency disturbing potential T^ℓ is computed using the one-step method described in Sect. 2.1 and high-frequency airborne GDVs denoted as $\delta\mathbf{g}^\ell$, see Eq. (6). They are obtained from observed GDVs that are reduced for low-frequency GDVs $\delta\mathbf{g}_\ell$ synthesized from GGM. The low-frequency disturbing potential T_ℓ is then added to the high-frequency disturbing potential T^ℓ. This process, known in geodesy as remove-compute-restore, can be formalized as follows:

$$\begin{aligned} \delta\mathbf{g}^\ell(r,\Omega) &= \delta\mathbf{g}(r,\Omega) - \delta\mathbf{g}_\ell(r,\Omega), \\ \delta\mathbf{g}^\ell(r,\Omega) &= \frac{1}{4\pi R}\int\limits_{\Omega_G} T^\ell\left(R,\Omega'\right)\mathbf{P}^\ell(r,\psi,R)\,\mathrm{d}\Omega', \\ T\left(R,\Omega'\right) &= T_\ell\left(R,\Omega'\right) + T^\ell\left(R,\Omega'\right). \end{aligned} \tag{18}$$

The high-frequency kernel function $\mathbf{P}^\ell$ is obtained by removing its low-frequency component

$$\begin{aligned} &\mathbf{P}^\ell(r,\psi,R) = \\ &\mathbf{P}(r,\psi,R) - \mathbf{P}_\ell(r,\psi,R) = \mathbf{P}(r,\psi,R) - \sum_{n=2}^{\ell}\left(\frac{R}{r}\right)^{n+2}(2n+1)\mathbf{V}_n(\alpha,\psi), \end{aligned} \tag{19}$$

where $\mathbf{V}_n(\alpha,\psi) = \left[\cos\alpha P_{n,1}(\cos\psi),\ \sin\alpha P_{n,1}(\cos\psi), (n+1)P_n(\cos\psi)\right]^T$. As no GGM is error-free, high-frequency GDVs still contain some signal components that should be resolved by GGM. This issue is addressed by modifying the integral function, see Sect. 2.3.

The high-frequency kernel function $\mathbf{P}^\ell$ must be adjusted according to the actual frequency content of measured GDVs. However, determining the spectral content of measured airborne GDVs is not a trivial task as it is affected by various computational errors (related to discretization and topographic effects) and raw signal filtering. This study employs the high-frequency integral kernels as defined in Eq. (19) without introducing any significant numerical inaccuracies.

2.3 Numerical evaluation of integral equations

The numerical evaluation of Eq. (6) requires in theory global integration of continuous GDVs which is not possible. To resolve this issue, the global integration domain Ω_G is divided into near-zone (Ω_0) and far-zone ($\Omega_G - \Omega_0$) integration domains. The near-zone integration domain is defined as a spherical cap centered at the computation point with spherical radius ψ_0 defined by the extent of available GDVs. Its contribution is computed using numerical integration. The complementary far-zone integration domain represents the contribution of GDVs outside the spherical cap that is computed using GGM.

Only discrete values of measured GDVs are available in the near zone; therefore, the integral in Eq. (6) must be discretized for numerical solution. The limited spectral content (due to signal filtering) of high-frequency airborne GDVs and discretization of surface integrals stabilize numerical solutions of Eq. (6). However, further regularizations can be required (e.g., Tikhonov's method), see Sect. 3 for details. Components of the high-frequency kernel function $\mathbf{P}^\ell$ vary over small increments of the spherical distance ψ_0. To ensure their accurate evaluation for each cell within the near zone, we employ an analytical approach based on local planar approximation. This approximation, adapted from Goli et al. (2019a), replaces the point value of the kernel function at the center of each cell with the mean value computed by analytical integration in a local Cartesian coordinate system. Derivation of the kernel components and validation of this approximation are provided in Appendix A.

Although Fig. 1 (and the corresponding figure for the vertical kernel component P_U not presented herein) indicates that the integral kernel components decay rapidly with the increasing spherical distance, this is not the case for the high-frequency kernel function $\mathbf{P}^\ell$, and particularly not for its vertical component P_U^ℓ (Goli et al. 2019b). This means that the high-frequency kernel components must be modified to minimize the far-zone contribution (truncation error), since GGM is assumed to be less accurate (within the respective degree band) than local airborne gravity observations. The integral equation in Eq. (18) can be written using a modified high-frequency kernel function $\widetilde{\mathbf{P}}^\ell$ and global integration domain Ω_G divided into the near and far zones

$$\begin{aligned} \delta\mathbf{g}^\ell(r,\Omega) &= \frac{1}{4\pi R}\int_{\Omega_0} T^\ell\left(R,\Omega'\right)\tilde{\mathbf{P}}^\ell(r,\psi,R)\,\mathrm{d}\Omega' \\ &+ \frac{1}{4\pi R}\int_{\Omega_G-\Omega_0} T^\ell\left(R,\Omega'\right)\tilde{\mathbf{P}}^\ell(r,\psi,R)\,\mathrm{d}\Omega', \end{aligned} \tag{20}$$

where the second integral on the right-hand side of Eq. (20) represents the far-zone contribution that is minimized through kernel modification. It is calculated using a GGM, which is considered less accurate than airborne GDV in their frequency band. Novák (2003) applied the deterministic method of Vaníček & Kleusberg (1987) to modify the high-frequency vertical kernel function P_U^ℓ by minimizing the far-zone contribution

$$\begin{aligned}\tilde{P}_U^\ell(r,\psi,R;\psi_0) &= P_U^\ell(r,\psi,R)\\ &- \sum_{n=0}^{\ell}\frac{2n+1}{2}t_n(R,\psi_0,r)P_n(\cos\psi),\end{aligned} \tag{21}$$

where $\widetilde{P}_U^\ell$ is the modified high-frequency vertical kernel component. Modification coefficients t_n are derived in Appendix B. The far-zone contribution $\delta g_U^{\ell,FZ}$ for the high-frequency vertical component of GDV is evaluated using a GGM as follows:

$$\delta g_U^{\ell,FZ}(r,\Omega) = \frac{GM}{R^2}\sum_{n=\ell+1}^{L}\left(\frac{r}{R}\right)^{n+1}V_n^U(r,\psi_0,R)T_n(\Omega), \tag{22}$$

where GM denotes the product of the universal gravitational constant G and the Earth's mass M, T_n is the n-th degree surface spherical harmonic of the disturbing potential, and L is the maximum degree of the far-zone contribution defined as degree beyond which it is negligible. V_n^U are truncation coefficients computed by

$$V_n^U(r,\psi_0,R) = \int\limits_{\psi_0}^{\pi}\tilde{P}_U^\ell(r,\psi,R;\psi_0)P_n(\cos\psi)\sin\psi\,\mathrm{d}\psi,\ \ell+1\le n\le L. \tag{23}$$

More details regarding the evaluation of the far-zone contribution in Eq. (22) can be found in Appendix C.

Only the isotropic part of the high-frequency horizontal kernel components P_E^ℓ and P_N^ℓ, denoted as P_H^ℓ, is modified. This isotropic part reads

$$P_H^\ell(r,\psi,R) = \frac{3R^3\left(r^2-R^2\right)}{L^5(r,\psi,R)}\sin\psi - \sum_{n=1}^{\ell}\left(\frac{R}{r}\right)^{n+2}(2n+1)P_{n,1}(\cos\psi). \tag{24}$$

The modified high-frequency horizontal kernel component can be expressed as follows:

$$\tilde{P}_H^\ell(r,\psi,R;\psi_0) = P_H^\ell(R,\psi,r) - \sum_{n=1}^{\ell}k_n q_n(R,\psi_0,r)P_{n,1}(\cos\psi), \tag{25}$$

where $k_n = \frac{1}{\int_0^\pi\left[P_{n,1}(\cos\psi)\right]^2\sin\psi\mathrm{d}\psi} = \frac{2n+1}{2n(n+1)}$ is the inverted norm of the Legendre function $P_{n,1}$, and modification coefficients q_n are also derived in Appendix B.

Far-zone contributions for the horizontal components of GDV can be computed by

$$\begin{bmatrix}\delta g_N^{\ell,FZ}(r,\Omega)\\ \delta g_E^{\ell,FZ}(r,\Omega)\end{bmatrix} = \frac{GM}{2R^2}\sum\nolimits_{n=0}^{L}\frac{1}{n(n+1)}\left(\frac{r}{R}\right)^{n+1}V_n^H(r,\psi_0,R)\begin{bmatrix}\frac{\partial T_n(\Omega)}{\partial\varphi}\\ \frac{1}{\cos\varphi}\frac{\partial T_n(\Omega)}{\partial\lambda}\end{bmatrix}, \tag{26}$$

where the truncation coefficients of the horizontal components have the following spatial form:

$$V_n^H(r,\psi_0,R) = \int_{\psi_0}^{\pi}\tilde{P}_H^\ell(r,\psi,R;\psi_0)P_{n,1}(\cos\psi)\sin\psi\,\mathrm{d}\psi,\ \ell+1\le n\le L. \tag{27}$$

More details regarding evaluation of far-zone contributions in Eq. (26) can be found in Appendix C.

3 Estimation of the high-frequency disturbing potential

Discretized forms of the integral equations are used for their numerical solution. The discrete form for the near-zone contributions of Eq. (6) results in the system of linear equations

$$\mathbf{A}_N\mathbf{x} = \mathbf{b}_N + \mathbf{r}_N;\ \mathbf{A}_E\mathbf{x} = \mathbf{b}_E + \mathbf{r}_E;\ \mathbf{A}_U\mathbf{x} = \mathbf{b}_U + \mathbf{r}_U, \tag{28}$$

where $\mathbf{x}$ is the vector with unknown values of the high-frequency disturbing potential on the sphere, and $\mathbf{b}_N$, $\mathbf{b}_E$, and $\mathbf{b}_U$ are vectors containing measured high-frequency components of GDVs ($\mathbf{b}$) reduced for far-zone contributions. Vectors $\boldsymbol{r}_N$, $\boldsymbol{r}_E$, $\boldsymbol{r}_U$ represent observation errors of the GDV components. Values of the high-frequency modified horizontal kernel $\widetilde{P}_H^{\ell}$ in Eq. (25) are elements of the design matrices $\mathbf{A}_N$ and $\mathbf{A}_E$, and values of the modified high-frequency vertical kernel function $\widetilde{P}_U^{\ell}$ in Eq. (21) are entries of the design matrix $\mathbf{A}_U$. If the design matrices $\mathbf{A}_N$, $\mathbf{A}_E$ and $\mathbf{A}_U$ (submatrices of $\mathbf{A}$) have the full rank, one can form a system of linear equations and find its solution, e.g., by the least-squares method. The numerical stability of the solution to the vector-valued one-step method in its discretized form is affected by various factors, including discretization of the integration domains, spatial distribution of GDVs, their dominant high-frequency content (e.g., due to rugged topography), noise characteristics, and locations where the unknown disturbing potential is sought. Although the spectrally limited content of airborne GDVs and discretization of integration domains help to stabilize the numerical solutions, further regularization may still be required.

The system of linear equations in Eq. (28) can be solved using either direct or iterative methods. Iterative methods do not require inverting the normal matrix; instead, the solution is refined in each iteration by calculating the product of the matrix with the vector. In this study, we utilize the iterative LSQR method (least-squares with QR factorization), known for its efficiency in handling large-scale, sparse systems (Paige and Saunders 1982). However, iterative methods, such as LSQR, converge to the least-squares solution which can be problematic for ill-posed problems due to the observation noise. Therefore, it is crucial to stop the iterative process after a few steps, before the solution gets significantly corrupted by the noise. Various criteria, such as the discrepancy principle, generalized cross-validation or the L-curve can be used as a stopping rule, although they may yield different results (Goli et al. 2018). Hence, selecting an appropriate criterion for determining the optimal stopping rule is vital.

Iterative solvers naturally incorporate regularization through the iteration count: in this context, the dimension of the Krylov subspace acts as the regularization parameter. The discrepancy principle offers a simple and effective stopping rule, iterations are terminated once the residual norm falls below the estimated noise level in the observations. Since the true noise level is not known a priori, we adopt a straightforward, data-driven strategy: each iterative geoid solution is compared with an external geoid model, GNSS/leveling-derived where available, and the optimal iteration is selected based on the minimum STD misfit.

As the same GNSS/leveling data are also used for accuracy assessment, the validation is not entirely external, and the reported accuracy may reflect some internal optimization. In the absence of a separate, independent dataset, this approach still offers meaningful insight into the model's relative performance.

Another important aspect in combining the three GDV components is to determine their weights. The standard approach for assigning weights to observations in solving linear equations is the variance component estimation method (Koch and Kusche 2002; Xu et al. 2006). However, addressing the impact of weights and their estimation, while solving the equations is also beyond the objectives of this study. It is worth noting that in the state-of-the-art airborne gravity surveys, the horizontal and vertical components of the gravity vector are measured with a similar accuracy, which reduces the significance of weights on the final solution.

4 Topographic effects on GDVs and disturbing potential

As previously mentioned, Poisson's integral equation and its gradient can be used only in mass-free space, meaning that gravitational effects of all masses outside the geoid (including topography) must be removed from observed gravity. Helmert's and No Topography (NT) computation spaces are commonly used for this purpose (Vaníček et al. 2004; Vajda et al. 2020). In the Helmert space, the gravitational effect of topographic mass is balanced by the gravitational effect of a thin mass layer on (or inside) the sphere approximating the geoid and their difference is then used to reduce GDVs. In contrast, the NT space removes the gravitational effect of topographic masses from observed GDVs. This approach generally results in a smoother gravity field compared to Helmert's field (Vaníček et al. 2004). As high-frequency GDVs are used when solving the Poisson integral equation, topographic effects must reflect their limited spectral content.

By defining the high-frequency disturbing potential in the NT space $T^{NT,\ell}$

$$T^{NT,\ell}(r,\Omega) = T^{\ell}(r,\Omega) - V^{t,\ell}(r,\Omega), \tag{29}$$

where $V^{t,\ell}$ is the high-frequency gravitational potential of the topographic masses. The gradient of Eq. (29) gives the high-frequency NT gravity disturbance vector $\delta\boldsymbol{g}^{NT,\ell}$

$$\nabla T^{NT,\ell} = \nabla T^{\ell} - \nabla V^{t,\ell} \rightarrow \delta \boldsymbol{g}^{NT,\ell} = \delta \boldsymbol{g}^{\ell} - \boldsymbol{g}^{t,\ell},$$

where $\boldsymbol{g}^{t,\ell}$ is a vector-valued high-frequency direct topographic effect on the high-frequency gravity vector $\delta\boldsymbol{g}^{\ell}$. In the restore step, the high-frequency geoidal height in the real space can be computed by applying the high-frequency indirect topographic effect $N^{t,\ell}$ on the high-frequency NT geoid $N^{NT,\ell}$

$$N^{\ell}(\Omega) = N^{NT,\ell}(r,\Omega) + \frac{V^{t,\ell}(r,\Omega)}{\gamma_0} = N^{NT,\ell}(r,\Omega) + N^{t,\ell}. \qquad (30)$$

Both direct and indirect topographic effects must have the frequency content adjusted according to those of the high-frequency airborne GDVs $\delta\boldsymbol{g}^{\ell}$ and the recovered high-frequency geoidal heights $N^{NT,\ell}$ computed by solving Poisson's integral equations, respectively. For this purpose, we use the spectral model of global topography dV_ELL_Earth2014_5480 by Rexer (2017). This approach has an alternative that is based on numerical integration of topographic effects using DEMs, followed by their low-pass filtering to remove high frequencies and application of a global spectral model to remove low frequencies.

5 Numerical results

5.1 GGM-based airborne GDVs

Derivations in Sect. 4 were verified using a closed-loop test over the 1-cm geoid area in Colorado (USA) which is known for its challenging topography. This area has been extensively used in the context of local geoid modeling, particularly for the 1-cm geoid experiment (Wang et al. 2021). Input gravity data cover a geographic area bounded by $-109^{\circ} < \lambda < -102^{\circ}$ W and $35^{\circ} < \varphi < 39^{\circ}$N, while the geoid computation area is represented by its central $5^{\circ} \times 3^{\circ}$ block. GGM-based GDVs were computed using XGM2019e (Zingerle et al. 2020) with 5 km cross-line spacing and 200 m along-line spacing, which for the aircraft speed of 55 m/s corresponds to a sampling interval of 3.6 s. Airborne GDVs were calculated on a gentle drape surface with the clearance of 300–500 m above the Earth's surface that has been tested for airborne surveys also in other areas. Closed-loop tests with GGM-based GDVs are used in this study, since they provide a well-controlled environment to test the formulated mathematical models and their software implementation, estimate numerical errors, and provide external errors of the solution using reference values of the sought parameters.

GGM-based high-frequency GDVs were calculated within the degree band of $n \in [361,5540]$. To add realistic noise, we analyzed the test airborne gravity vector survey on a profile over the Geoid Slope Validation Survey 2014 (GSVS14) in Iowa (Ferguson et al. 2017; Wang et al. 2017). Test observations are from repeated lines collected at two different heights of 500 and 2000m. The average aircraft (ground) speed is 58 m/s and observations were 'collected' at a 10Hz rate. The original observations are filtered by a Butterworth filter of half-amplitude at a full wavelength of 4km (corresponding to an effective resolution of approximately 2 km, defined here as half the cutoff wavelength, a common convention in geophysical signal processing; see, e.g., Wessel and Watts, 1988; Strykowski and Forsberg, 1998) at that flight speed. The average difference between each component of the observed GDVs for the two repeated flight Lines is 0.75 mGal which is considered as the noise level for the simulated GGM-based GDVs. We simulate the colored noise with the same magnitude to be added to these GDVs. This colored noise is generated using the sum of low-pass and band-pass filtered white noise sequences with a resultant standard deviation of 0.75 mGal that are subsequently low-pass filtered to the bandwidth of 1/80 Hz at half amplitude, or 4.4 km at the flight speed of 55 m/s. This implies a spatial resolution of approximately 2.2 km, again taken as half the cutoff wavelength. Our assumption of the noise magnitude is also aligned with the accuracy of the state-of-the-art airborne gravity surveys (Deng et al. 2020; Bidel et al. 2023).

Figure 2 shows variations of the three components of GGM-based high-frequency GDVs computed on a 5 km line spacing. This dataset represents input gravity observations for closed-loop tests, i.e., entries of the vector $\mathbf{b} = [\mathbf{b}_N, \mathbf{b}_E, \mathbf{b}_U]^T$. We also generate GGM-based high-frequency geoidal heights using XGM2019e and the same degree band to be applied as reference values for solutions of the integral equations; they are denoted as $\mathbf{x}^{\text{ref}}$. The high-frequency disturbing potential T^{ℓ} on the 2 arc-min equiangular grid on the sphere is estimated by inverting the scattered components of GGM-based GDVs. The results are then converted to the geoidal heights using Bruns's formula.

5.1.1 Inversion results

First, high-frequency geoidal heights are determined by inverting only the high-frequency vertical GDV component, considered herein as the "traditional approach". We test various parameters to estimate optimal values for degree ℓ of the kernel modification and radius of the spherical cap ψ_0 and compare each solution with the reference geoidal heights $\mathbf{x}^{\text{ref}}$, computed using XGM2019e. Our computations indicate that the best values for ℓ and ψ_0 are 360 and $30'$, respectively. Using these parameters, computations are repeated using horizontal GDV components. It is important to note that inverting any single horizontal component does not yield any meaningful

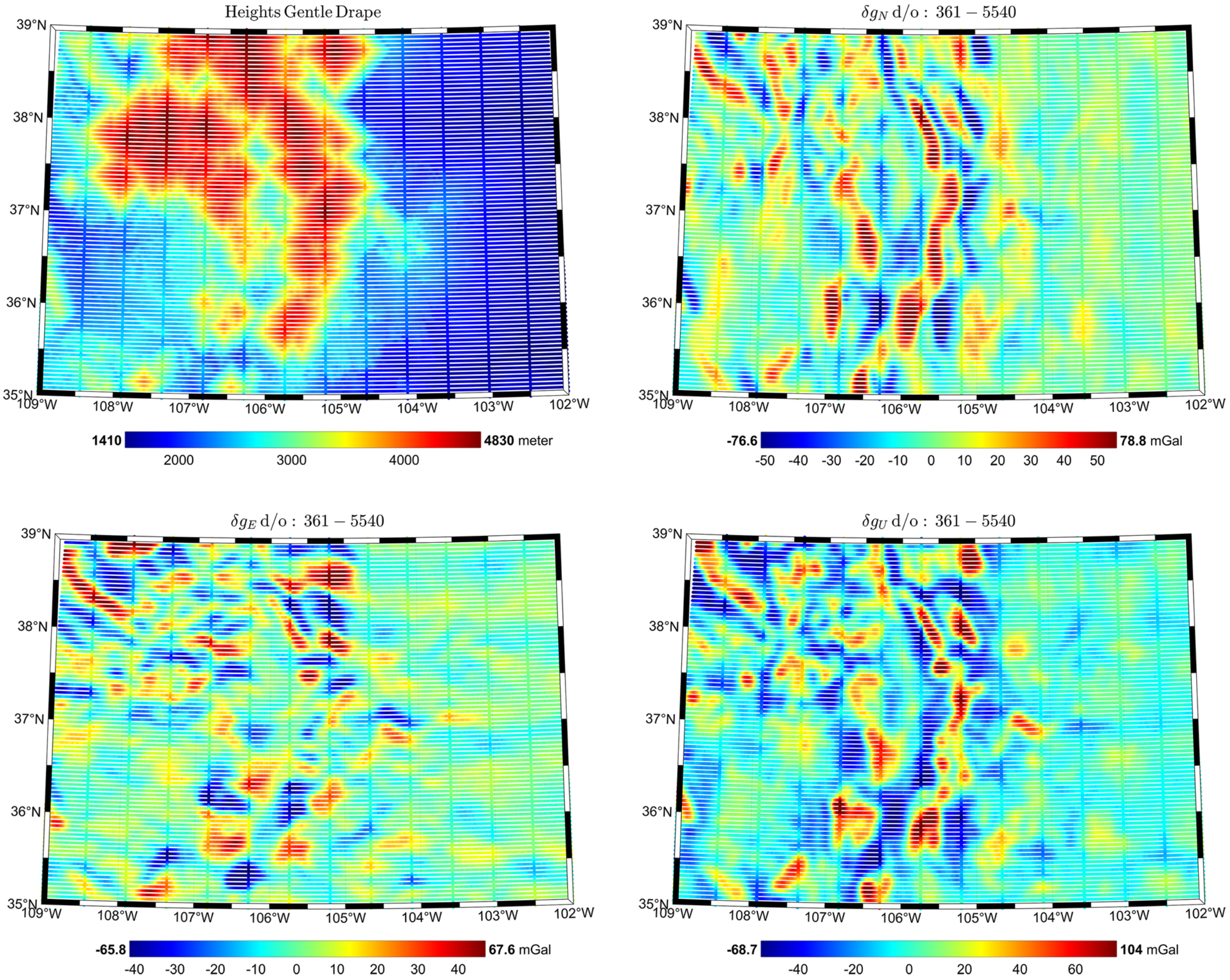

Fig. 2 Heights (m) of the gentle drape surface over Colorado and three components of high-frequency GDVs (mGal) computed from XGM2019e within degrees [361,5540]

solution of the geoidal height. However, this is not the case for combination of two horizontal GDV components. Their results are better than those obtained using only the vertical component, with the optimal values of ℓ and ψ_0 still being 360 and 30$'$, respectively. Notably, the accuracy obtained by combining horizontal GDV components is 3.4 cm which is roughly 40% better than when only the vertical component is used (5.8 cm). Inversion of the horizontal GDV components into the geoidal height is equivalent to using deflections of the vertical for geoid modeling. Depending on the computation parameters, such as the integration cap-radius, maximum degree of the reference field, and noise characteristics of the input gravity vector components, the resulting geoid model based on all three components of the disturbing gravity vector can yield superior accuracy compared to the geoid model derived using only the vertical component. The deflection of the vertical at flight level estimates the gravity signal between the flight lines which are relatively sparse to keep airborne gravity surveys cost-effective.

Table 1 Geoid accuracy (m) resulting from inversion of δg_U^ℓ, two horizontal components, and the full airborne gravity vector $\boldsymbol{\delta g}^\ell$ for $\psi_0 = 30^{/prime}$ and $\ell = 360$

Component	Min	Max	Mean	Std
Vertical	−0.572	0.604	0.001	0.058
Two horizontal	−0.403	0.277	−0.003	0.034
All three	−0.230	0.276	0.000	0.027

Final calculations are carried out using full GDVs including far-zone contributions; see Sect. 5.1.2 for more details. The accuracy of the computed high-frequency geoidal heights based on all three high-frequency GDV components improves by more than 50% compared to using only the vertical component. Table 1 provides statistics of the geoid errors obtained using only the horizontal and all three components of $\delta \mathbf{g}$ compared to the "traditional approach".

Although the vertical component of the gravity disturbance vector is typically used for geoid determination, the combination of both horizontal components resulted in a more accurate geoid recovery in our simulation study. This may be attributed to the directional completeness of the horizontal field: each component alone provides only partial information, but combined, they offer full sensitivity to lateral gravity variations. Extreme values of the geoid errors in Table 1 can be attributed to several factors. First, a 1 arc-min equiangular grid was employed, which, although yielding inherently unstable solutions, was chosen to test the developed mathematical model and implemented software under a worst-case scenario for geoid determination used in this study. Second, irregularly distributed data and 5 km flight line spacing were designed to replicate real-world conditions, in contrast to regular grid simulations used in other studies, such as Deng et al. (2020).

5.1.2 Far-zone contributions

In this section, we test formulations of the far-zone contributions to high-frequency GDVs recovered by solving the integral equations. For this purpose, the far-zone contributions are calculated using two scenarios: with and without kernel modifications. Additionally, the impact on the estimated geoidal height is assessed for all three GDV components. High-frequency far-zone contributions are computed for vertical and horizontal components of GDVs using Eqs. (22) and (26), and XGM2019e up to degree 720, because the experiment shows that higher degrees have only negligible magnitudes. Far-zone contributions to the components δg_E^ℓ, δg_N^ℓ, and δg_U^ℓ are shown in Fig. 3 for both the modified kernel ($\ell = 360$) and unmodified kernel and for the spherical cap with radius $\psi_0 = 30'$.

Table 2 Geoid accuracy from inversion of GGM-based high-frequency GDVs using modified and unmodified kernels (m)

Kernel function	Min	Max	Mean	Std
Unmodified	−0.578	0.624	0.001	0.062
Unmodified + far zone	−0.299	0.436	0.002	0.035
Modified	−0.235	0.277	0.000	0.027
Modified + far zone	−0.230	0.276	0.000	0.027

The lower panel of Fig. 3 shows that neglecting the far-zone contributions in the solutions based on unmodified kernel functions can lead to significant errors, emphasizing the necessity of kernel modifications even for ultra-high-resolution GGMs. Standard deviations of the far-zone contributions are, respectively, 2.4, 1.7, and 2.3 mGal for the north, east, and vertical high-frequency

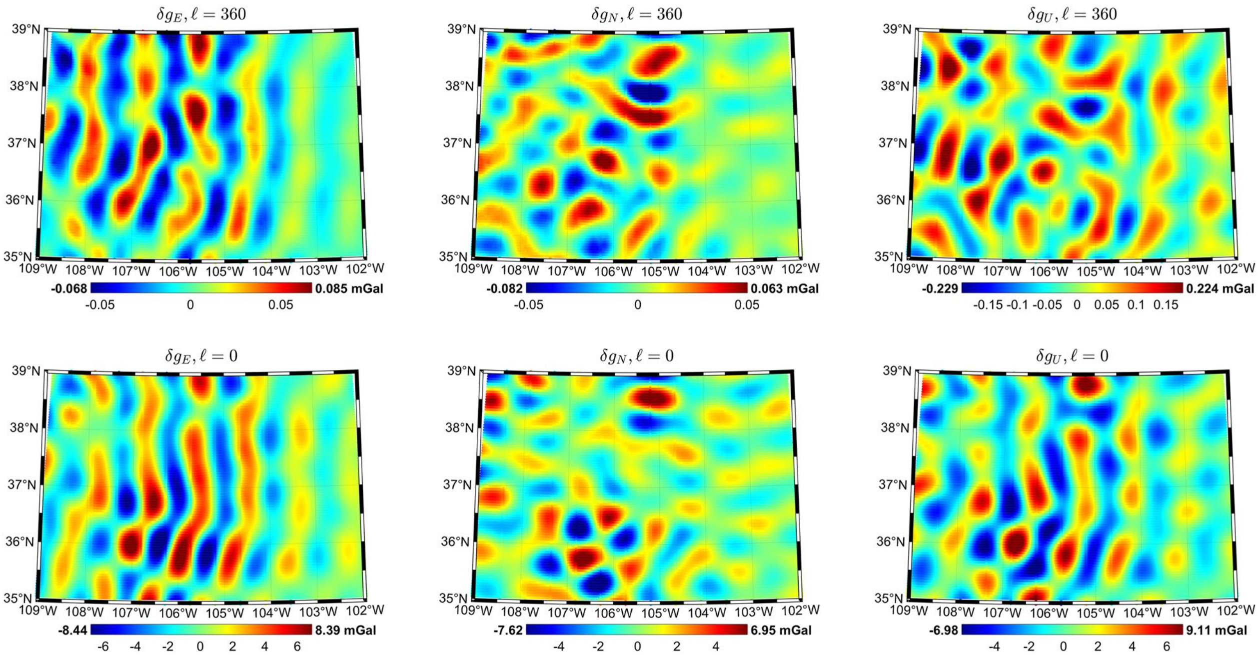

Fig. 3 Far-zone contributions of high-frequency GDV components (mGal) for the spherical cap $\psi_0 = 30'$, upper panels for the modified kernels ($\ell = 360$) and lower panels for the unmodified kernels

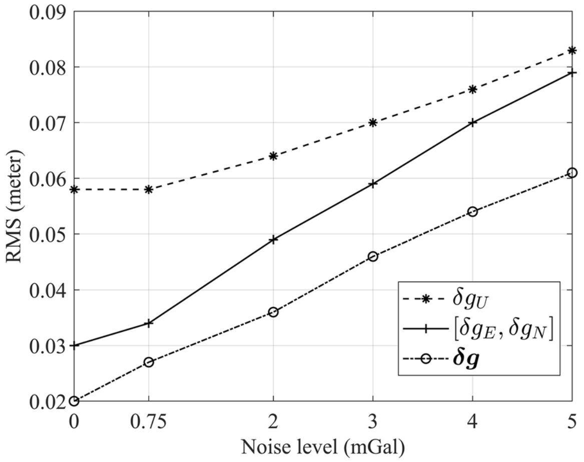

Fig. 4 Geoid errors for different noise magnitudes of GDV components

GDV components. Table 2 then compares estimated geoidal heights for four cases: with/without kernel modification and with/without far-zone contributions when compared with the reference geoidal heights $\mathbf{x}^{\mathrm{ref}}$ computed again using XGM2019e. Their differences confirm that incorporating far-zone contributions improves the accuracy of the recovered geoidal heights, but kernel modification remains essential for achieving superior accuracy.

5.1.3 Noise-free and noisy GDVs

Observation noise is an inherent part of airborne gravity data and its effect on geoid determination has been repeatedly discussed in the literature (Bayoud 2001; Liu et al. 2015; Zhao et al. 2018; Li et al. 2022). In this contribution, all computations were initially performed using the colored noise of 0.75 mGal for the GDV components as described in Sect. 5.1. To evaluate the impact of the varying noise magnitude, we conducted additional simulations with GDVs contaminated by a colored noise ranging from 0 to 5 mGal. Figure 4 illustrates the relationship between geoid accuracy and noise magnitude. Comparing the RMS of geoidal heights computed with noise-free data (first points on the Y axis of Fig. 4) with those when 0.75 mGal noise is added confirms that such a noise decreases the geoid accuracy by only a few millimeters in all tested scenarios, with the most pronounced effect ($\sim$ 7 mm) observed when using all GDV components. The vertical component is less sensitive to the increasing noise than horizontal GDV components. It is important to note that the simulations assume the same magnitude of the colored noise across all GDV components which does not always hold true in practice.

5.1.4 Inversion of NT GDVs

XGM2019e is a high-resolution global gravity model (d/o 5399) derived by combining observed and topographically derived gravity data. The topographic gravity were computed using Earth2014 model (Rexer 2017). To perform the computations in a mass-free space, vector-valued high-frequency direct and indirect topographic effects are calculated using the spectral model of global topography dV_ELL_Earth2014_5480 within the degree band of $n \in [361{,}5480]$. The high-frequency NT GDV is computed by applying the high-frequency direct topographic effects to GGM-based high-frequency GDV as described in Sect. 5.1. Figure 5 shows the east, north, and vertical components of the high-frequency NT GDV.

Figures 2 and 5 demonstrate that the high-frequency direct topographic effects computed using the model

Table 3 Geoid errors (m) resulting from inversion of NT GDVs for $\psi_0 = 30^{/prime}$ and $\ell = 360$

Component	Min	Max	Mean	Std
Vertical	−0.259	0.222	0.000	0.021
Two horizontal	−0.086	0.104	−0.001	0.014
All three	−0.074	0.072	−0.001	0.010

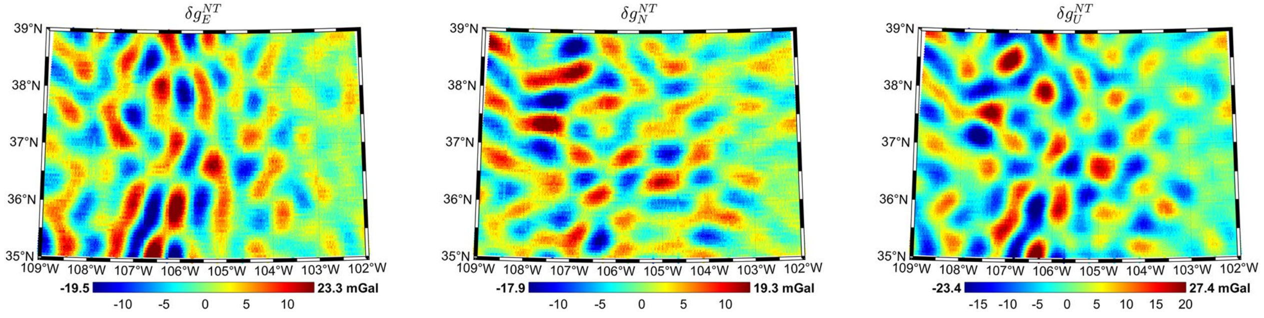

Fig. 5 Components of high-frequency NT GDVs (mGal)—GGM-based data

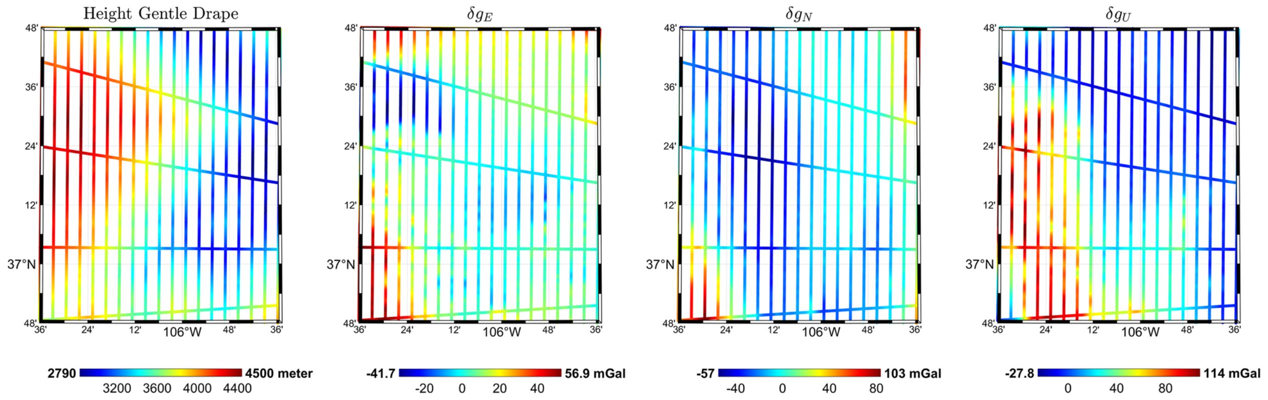

Fig. 6 Heights (m) of flight lines and observed GDV components (mGal) in Colorado

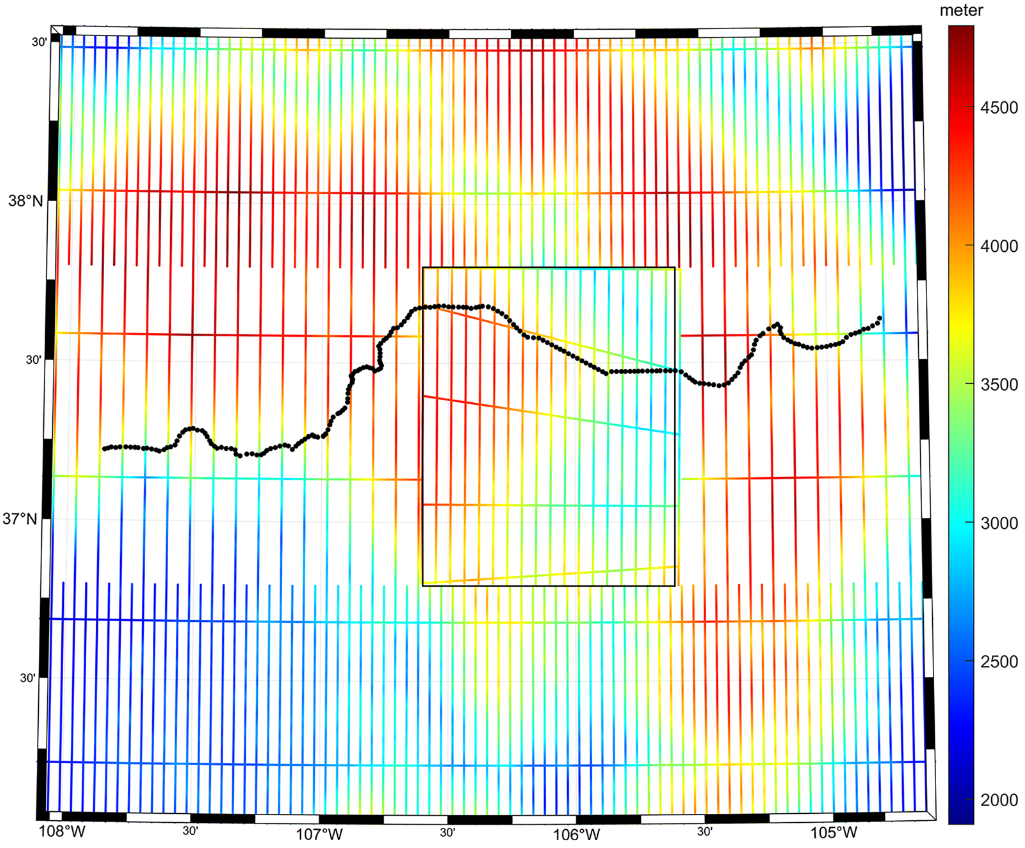

Fig. 7 Location of observed GDVs (black rectangle), extended area, and GSVS17 GNSS-leveling line (black line)

dV_ELL_Earth2014_5480 reduce the high-frequency content of GDVs and should improve numerical stability of the one-step method. To investigate this issue further, high-frequency NT geoidal heights are computed using the one-step method with vertical, two horizontal and all three high-frequency components of NT GDVs. Statistics of the geoid errors (estimated minus reference value) can be found in Table 3. Comparing these errors with values in Table 1 indicates that applying the one-step method in the NT space significantly reduces the geoid errors by nearly a factor of three. Standard deviations reported in Table 3 correspond to internal errors of the computational scheme due to discretization of surface integrals, truncation errors related to finite computation areas and

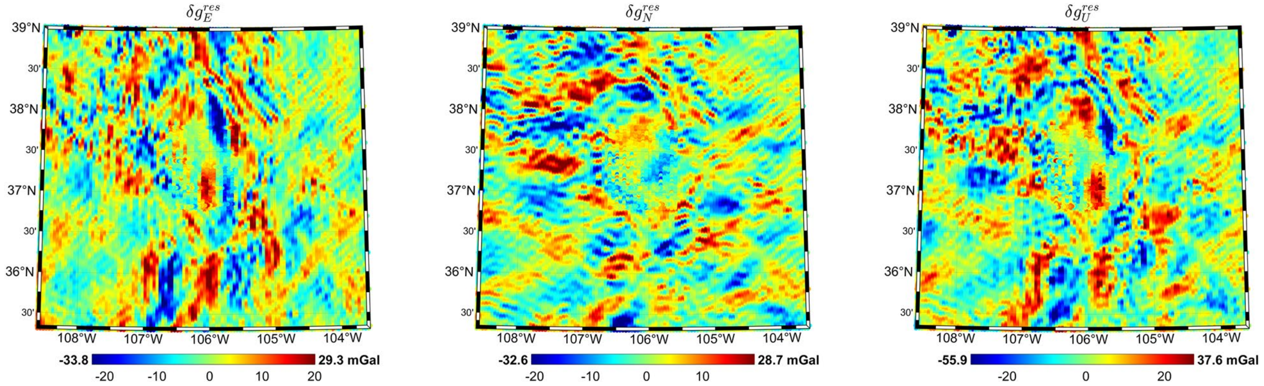

Fig. 8 Three components of the high-frequency GDVs in the NT space (mGal)—real data

numerical instabilities of the downward continuation process. Minor discrepancies could also arise from resolution and coverage of input GDVs or residual inconsistencies in observation and data processing.

5.2 Real airborne gravity data

To test the computational scheme further, real airborne GDVs collected by Sander Geophysics were used in this study. Airborne GDVs were collected using the Airborne Inertially Referenced Gravimeter (AIRGrav) mounted on Cessna 208B Grand Caravan aircraft over the 1 × 1 arc-deg

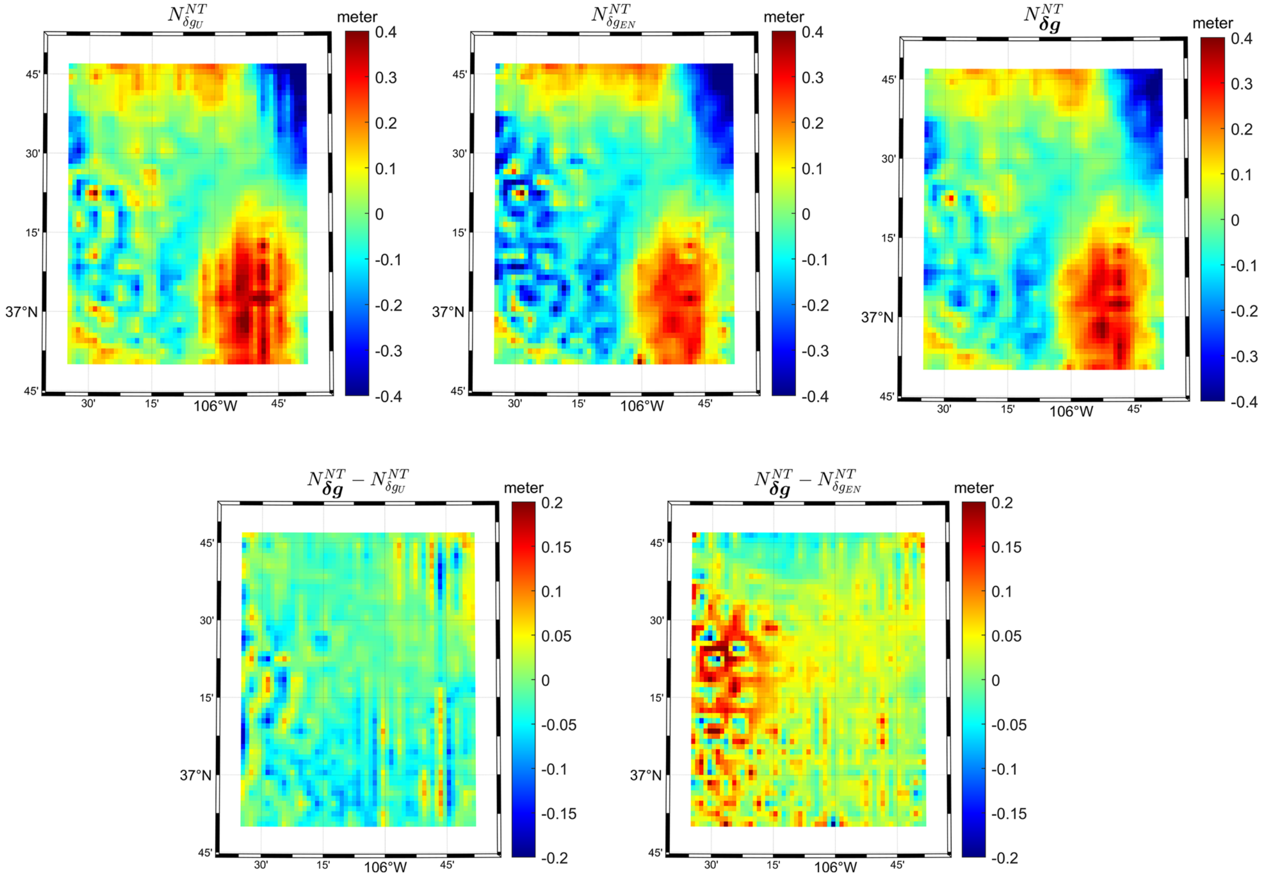

Fig. 9 High-frequency NT geoidal heights computed using $\boldsymbol{\delta g}^{\ell}$, δg_{EN}^{ℓ} and δg_{U}^{ℓ}, and their differences (m)

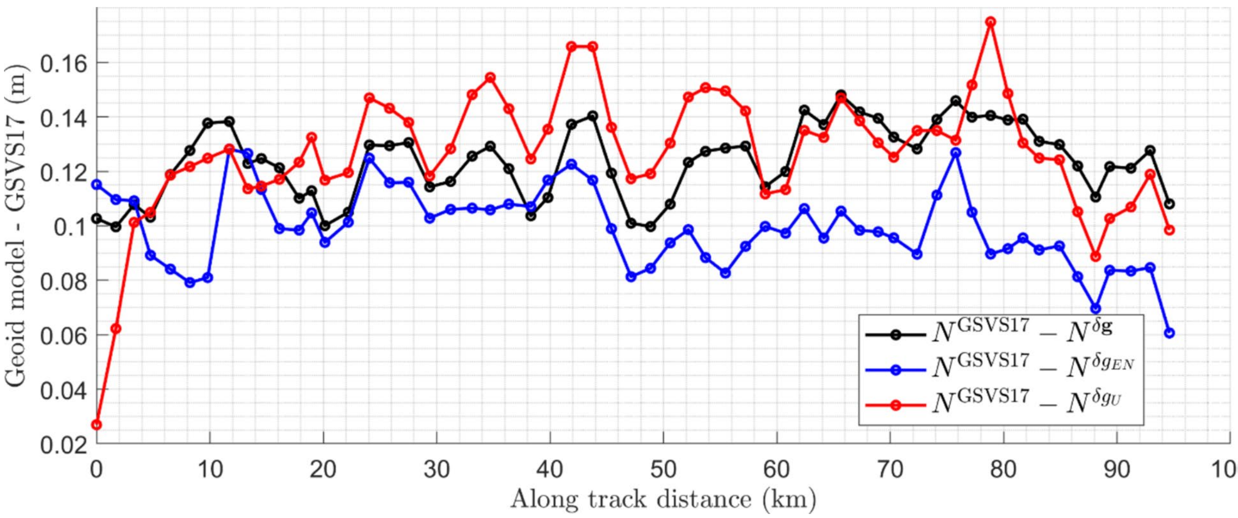

Fig. 10 Differences between the reference geoidal heights at GSVS17 profile benchmarks and geoidal heights computed by the one-step method using vertical, two horizontal and all three components (m)

Table 4 Statistics of the differences between the geoidal heights from inversion of NT GDVs and reference GSVS17 geoidal heights for $\psi_0 = 30^{/prime}$ and $\ell = 360$ (m)

Component	Min	Max	Mean	Std
Vertical	0.027	0.175	0.127	0.023
Two horizontal	0.061	0.128	0.099	0.014
All three	0.100	0.148	0.124	0.013

area in the 1-cm geoid test area in Colorado bounded by $-106.6^{\circ} < \lambda < -105.6^{\circ}\mathrm{W}\ and\ 36.8^{\circ} < \varphi < 37.8^{\circ}\mathrm{N}$ along a gentle drape surface that smoothly followed the Earth's surface while maintaining a clearance of 500–1800 m. Survey Lines were spaced 5 km apart, with four additional crossover Lines to ensure consistency and validate the measurements. The average flight speed was 60 m/s providing an effective spatial resolution of 1.92 km for gravity observations. The gravity observations here were filtered as in Sect. 5.1. Figure 6 shows the flight height and each component of the collected GDVs.

Due to the Limited data coverage and need to integrate over the 30' radius, the area with observed airborne GDVs is extended using GGM-based GDVs positioned along the gentle drape flight altitude with 5 km line spacing derived from the EIGEN-6C4 model (Förste et al. 2014) up to degree 2190. Please note that a different GGM is used here, because it provides a better fit to the observed GDVs, making it a more suitable choice for data extension. Since the data points along the flight Line are very close to each other, those within 500 m are excluded from the calculations. Figure 7 shows the flight altitude (on the designed gentle drape surface) of the gravity observations, and the Geoid Slope Validation Survey 2017 (GSVS17) data.

High-frequency GDVs are calculated by reducing the measured GDVs for low-frequency components derived from EIGEN-6C4 up to degree 360. The high-frequency direct topographic effects on GDVs computed using dV_ELL_Earth2014, corresponding to degrees 361–3600, are then applied to obtain the high-frequency NT GDVs, see Fig. 8. Our calculations indicate that the direct topographic effects on GDV components for degrees above 3600 do not further smooth the GDV components.

Finally, after correcting the high-frequency NT GDVs for their far-zone contributions using $\psi_0 = 30'$ and $\ell = 360$, the high-frequency geoidal heights in the NT space are computed by the one-step method. Figure 9 presents the high-frequency NT geoidal heights computed using $\boldsymbol{\delta g}^{NT,\ell}$, $\delta g_{EN}^{NT,\ell}$ and $\delta g_{U}^{NT,\ell}$ along with their respective differences. Standard deviations of the differences $N_{\boldsymbol{\delta g}}^{NT,\ell} - N_{\delta g_{EN}}^{NT,\ell}$ and $N_{\boldsymbol{\delta g}}^{NT,\ell} - N_{\delta g_{U}}^{NT,\ell}$ are, respectively, 5.6 and 4.1 cm, which is significant when one seeks the sub-cm accurate geoid.

In the restore step, the geoidal heights in the real space are obtained by adding the low-frequency geoidal heights and high-frequency indirect topographic effects. They are then compared with the reference Geoid Slope Validation Survey 2017 (GSVS17) data, with 56 out of 222 GSVS17 stations located within the computation area. Note that there are only handful of historical GPS-leveling benchmarks available in the test area, for which the accuracy is not comparable either with the GSVS17 values or the level of accuracy of the computed geoid models in this study; therefore, they are not included (Wang et al. 2021).

Figure 10 shows differences between the reference GSVS17 geoidal heights, and the geoidal heights estimated using the one-step method with the high-frequency vertical component δg_U^ℓ, two horizontal components δg_{EN}^ℓ, and the full GDV vector$\boldsymbol{\delta g}^\ell$. Table 4 presents statistics of the differences that indicate the accuracy of the individual solutions. The geoidal heights obtained using the horizontal components and the full GDV vectors are approximately one centimeter better than that obtained using only the vertical component. The accuracy of the geoidal heights derived using the full GDV and two horizontal components is nearly identical. However, to fully demonstrate the effectiveness of the horizontal components in improving the accuracy of the estimated geoidal heights, a more uniform distribution of GNSS/leveling control points in the region is needed. To verify our solutions further, we compare the final realization of the North American-Pacific Geopotential Datum of 2022, i.e., GEOID2022 model, published by the US National Geodetic Survey, against the same 56 GSVS17 stations used as reference in this study. The standard deviation of this comparison is 1.5 cm, which is larger than the accuracy of the best geoid model computed in our study.

6 Conclusions

The computational scheme for determination of a local geoid model using airborne GDVs is formulated in this study. The scheme is based on extending the existing one-step method for geoid determination using the vertical component of GDVs for two horizontal components. The comprehensive computational scheme contains formulas for deterministic modification of the kernel functions for all components of GDVs, far-zone contributions, and numerical solutions to the system of linear equations based on discretized surface integrals.

Numerical studies show that extending the one-step method for horizontal GDV components can significantly improve the accuracy of the local geoid model. Vaníček-Kleusberg's kernel modification method plays a crucial role in reducing truncation errors in the surface integrals. With this modification, far-zone contributions to the horizontal GDV components are reduced to just a few tens of μGals. However, applying the far-zone contributions does not further improve the geoid accuracy.

The computational scheme was evaluated using closed-loop tests under different scenarios with GGM-based high-frequency GDV components as input data. The advantage of using GGM-based GDVs is that corresponding values of the geoidal heights are known. Thus, numerical errors of the mathematical model and input data error propagation can be evaluated. Comprehensive statistics of the geoid accuracy include inversion of one vertical, two horizontal and all three GDV components, for both noise-free and noisy data. Utilizing only the high-frequency vertical component in the NT space results in an estimated geoid accuracy with a standard deviation of 2.1 cm. The joint inversion of the two high-frequency horizontal components in the NT space produces a geoid model with an improved accuracy of 1.4 cm. When all three GDV components are jointly inverted, the most accurate geoid model is obtained with a 50% improvement in the standard deviation (1.0 cm) relative to the geoid model based on the vertical GDV component alone. It should be noted here (for correct interpretation of the statistics) that there is an effect of the larger number of independent measurements (with random noise), which reduces the formal (internal) accuracy of the least-squares estimates.

Results obtained using real airborne GDV observations in the Colorado region confirm results based on GGM-based data. The standard deviation of the differences between the geoidal heights calculated using the vertical GDV component and reference GSVS17 geoidal heights is 2.3 cm, while for the horizontal GDV components, the same statistics is only 1.4 cm, indicating an improvement of nearly 40% (when the kernel function modified up to degree 360 is used). Additionally, the standard deviation based on the same differences for the geoidal heights based on all three GDV components is 1.3 cm. Unlike the closed-loop tests above, these statistics reflect the external accuracy of the results, where the reduced errors cannot be explained by a simple rule based on the square root of the number of observations used to solve the mathematical model. In other words, the improvement in the accuracy of the estimated geoids is real because of the increased number of uncorrelated measurements of input GDVs.

The statistics demonstrate that the presented computational scheme based on the one-step method for regional geoid determination is both effective and accurate. Thus, improvements in processing airborne GDVs, combined with advances in airborne gravity acquisition, allow the determination of regional high-frequency geoidal heights with cm-level accuracy using only airborne gravity data (with GGM supplying low frequencies). This accuracy level facilitates the use of airborne GDVs for regional geoid determination in rugged or inaccessible areas, e.g., Antarctica, without the need for costly and time-consuming surface gravity observations.

Appendix

Appendix A: Integral equations in planar approximation

Assuming a local Cartesian coordinate system with the origin in the center of the computation cell (φ_0, λ_0), we can define

$$\begin{bmatrix} x \\ y \end{bmatrix} = R\begin{bmatrix} \varphi - \varphi_0 \\ \cos\varphi(\lambda - \lambda_0) \end{bmatrix}. \tag{A1}$$

Using the planar approximation, we have $r^2 - R^2 = (R+h)^2 - R^2 \approx 2Rh$, $\mathrm{d}x = R\mathrm{d}\varphi$, and $\mathrm{d}y = R\cos\varphi\mathrm{d}\lambda$. With these approximations, Eq. (1) becomes

$$T(x,y,h) = \frac{h}{2\pi} \int_S T(x',y',0) \frac{1}{d^3} \mathrm{d}S, \tag{A2}$$

with the Euclidean distance $d = \left[(x-x')^2 + (y-y')^2 + h^2\right]^{\frac{1}{2}}$ and planar surface element $\mathrm{d}S = \mathrm{d}x'\mathrm{d}y'$. Horizontal components of Eq. (6) can be formulated in the planar approximation as follows:

$$\begin{bmatrix} \delta g_N(x,y,h) \\ \delta g_E(x,y,h) \end{bmatrix} = \frac{3Rh}{2\pi} \iint_S T(x',y',0) \frac{\sin\psi}{d^5} \begin{bmatrix} \cos\alpha \\ \sin\alpha \end{bmatrix} \mathrm{d}x'\,\mathrm{d}y'. \tag{A3}$$

Introducing the distance $d_0 = \left[(x-x')^2 + (y-y')^2\right]^{\frac{1}{2}}$, and for small ψ, we have $\psi = \sin\psi = \frac{d_0}{R}$, see Fig. 11, then

$$\begin{bmatrix} \delta g_N(x,y,h) \\ \delta g_E(x,y,h) \end{bmatrix} = \frac{3h}{2\pi} \iint_S T(x',y',0) \frac{d_0}{d^5} \begin{bmatrix} \cos\alpha \\ \sin\alpha \end{bmatrix} \mathrm{d}x'\,\mathrm{d}y'. \tag{A4}$$

In the local Cartesian system, we have

$$d_0 \begin{bmatrix} \cos\alpha \\ \sin\alpha \end{bmatrix} = \begin{bmatrix} x\prime - x \\ y' - y \end{bmatrix}, \tag{A5}$$

and

$$\begin{bmatrix} \delta g_N(x,y,h) \\ \delta g_E(x,y,h) \end{bmatrix} = \frac{3h}{2\pi} \iint_S T(x',y',0) \frac{1}{d^5} \begin{bmatrix} x' - x \\ y' - y \end{bmatrix} \mathrm{d}x'\,\mathrm{d}y', \tag{A6}$$

or

$$\begin{bmatrix} \delta g_N(x,y,h) \\ \delta g_E(x,y,h) \end{bmatrix} = \frac{1}{2\pi} \iint_S T(x',y',0) \begin{bmatrix} P_N^P(x,y,x',y',h) \\ P_E^P(x,y,x',y',h) \end{bmatrix} \mathrm{d}x'\,\mathrm{d}y', \tag{A7}$$

where P_N^P and P_E^P are the horizontal components of the vector-valued planar kernel function

$$\begin{bmatrix} P_N^P(x,y,x',y',h) \\ P_E^P(x,y,x',y',h) \end{bmatrix} = 3h\frac{1}{d^5}\begin{bmatrix} x\prime - x \\ y' - y \end{bmatrix}. \tag{A8}$$

The analytical solution of the integral in Eq. (A6) for the computation cell C is as follows:

$$\int_{x_1}^{y_1}\int_{y_1}^{y_2} \begin{bmatrix} P_N^P(x,y,x',y',h) \\ P_E^P(x,y,x',y',h) \end{bmatrix} \mathrm{d}x'\,\mathrm{d}y' = -h \left|\left| \begin{matrix} \frac{y'-y}{d\left[h^2+(x'-x)^2\right]} \\ \frac{x'-x}{d\left[h^2+(y'-y)^2\right]} \end{matrix} \right|_{x_1}^{x_2}\right|_{y_1}^{y_2},$$

where x_1, x_2, y_1, y_2 are the boundaries of the integration cell in the local Cartesian system.

The vertical derivative of the integral equation in Eq. (A2) is provided in Sec 2.1 of Goli et al. (2019a). It is given below for completeness

$$\delta g_Z(x,y,h) = \frac{1}{2\pi} \int_S T(x',y',0)\, P_Z^P(x,y,x',y',h)\mathrm{d}x'\mathrm{d}y', \tag{A9}$$

where the vertical component of the kernel function P_Z^P reads

$$P_Z^P(x,y,x',y',h) = \frac{d^2 - 3h^2}{d^5}.$$

The analytical solution of the integral in Eq. (A9) for the computation cell C is

$$\begin{aligned} &\int_{x_1}^{y_1}\int_{y_1}^{y_2} P_Z^P(x,y,x',y',h)\,\mathrm{d}x'\mathrm{d}y' \\ &= \left|\left| \frac{(x-x')(y'-y)(d^2+h^2)}{d\left[h^2+(x-x')^2\right]\left[h^2+(x-x')^2\right]} \right|_{x_1}^{x_2}\right|_{y_1}^{y_2}. \end{aligned} \tag{A10}$$

Appendix B: Modification coefficients of integral kernels

Molodensky-type modification coefficients t_n in Eq. (21) for vertical components can be determined by solving the

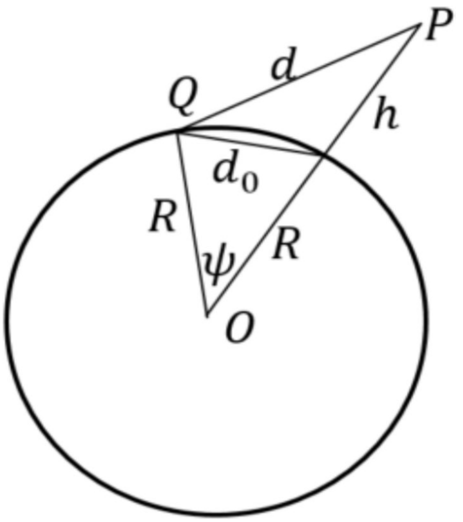

Fig. 11 Relation of the distance d_0 and spherical distance ψ

following system of linear equations (Vaníček and Kleusberg 1987):

$$\sum_{n=0}^{\ell} \frac{2n+1}{2} R_{n,m}(\psi_0) t_n(R,\psi_0,r) = \int_{\psi_0}^{\pi} P_U^{\ell}(r,\psi,R) P_m(\cos\psi)\sin\psi\,\mathrm{d}\psi,\, m \le \ell, \tag{A11}$$

with numerical coefficients $R_{n,m}$ determined by integration of a product of two Legendre functions

$$R_{n,m}(\psi_0) = \int_{\psi_0}^{\pi} P_n(\cos\psi)\, P_m(\cos\psi)\sin\psi\,\mathrm{d}\psi,\, m \le n. \tag{A12}$$

Recursive formulas for numerical evaluation of the coefficients $R_{n,m}$ can be found in Paul (1973). Here, we use the formula provided by Semernya and Skobelev (2019)

$$R^m_{n_1,n_2}(x) = \textstyle\int P_{n_1,m}(x) P_{n_2,m}(x)\,\mathrm{d}x = \frac{1-x^2}{(n_1-n_2)(n_1+n_2+1)} \left[P_{n_1,m}(x)\frac{\mathrm{d}P_{n_2,m}(x)}{\mathrm{d}x} - \frac{\mathrm{d}P_{n_1,m}(x)}{\mathrm{d}x}P_{n_2,m}(x)\right], n_1 \ne n_2, \tag{A13}$$

where $x = \cos\psi$. For $m = 0$ and $n \ne m$, the coefficients $R_{n,m}$ become

$$R_{n,m}(\psi_0) = \frac{1-x_0^2}{(n-m)(n+m+1)} \left[P_n(x_0)\left.\frac{\mathrm{d}P_m(x)}{\mathrm{d}x}\right|_{x=x_0} - P_m(x_0)\left.\frac{\mathrm{d}P_n(x)}{\mathrm{d}x}\right|_{x=x_0}\right], \tag{A14}$$

where $x_0 = \cos\psi_0$. For $n_1 = n_2 = n$ and $n > m$, coefficients $F^m_{n,n}$ can be computed using the following formula [ibid]:

$$F^m_{n,n}(x) = \frac{1}{n-m}\left\{ \frac{2n-1}{2n+1}\left[(n-m+1)F^m_{n+1,n-1}(x) + (n+m)F^m_{n-1,n-1}(x)\right] - (n+m-1)F^m_{n,n-2}(x)\right\}. \tag{A15}$$

Therefore, $R_{n,n} = F^0_{n,n}$ that yields for $n > 0$

$$R_{n,n}(\psi_0) = \frac{(2n-1)(n+1)}{n(2n+1)} R_{n+1,n-1}(\psi_0) + \frac{2n-1}{2n+1} R_{n-1,n-1}(\psi_0) - \frac{n-1}{n} R_{n,n-2}(\psi_0), \tag{A16}$$

with the seed value for the recurrence given as $R_{0,0}(\psi_0) = -(1+\cos\psi_0)$.

Molodensky-type modification coefficients q_n in Eq. (25) for horizontal components can be then solved by the following system of linear equations for $m \le \ell$:

$$\sum_{n=0}^{\ell} \frac{2n+1}{2n(n+1)} R^1_{n,m}(\psi_0) q_n(R,\psi_0,r) = \int_{\psi_0}^{\pi} P^{\ell}(r,\psi,R)\, P_{m,1}(\cos\psi)\sin\psi\,\mathrm{d}\psi, \tag{A17}$$

where $R^1_{n,m}$ reads

$$R^1_{n,m}(\psi_0) = \int_{\psi_0}^{\pi} P_{n,1}(\cos\psi)\, P_{m,1}(\cos\psi)\sin\psi\,\mathrm{d}\psi,\, m \le n. \tag{A18}$$

The coefficients $R^1_{n,m}$ can be derived from Eq. (A13) for $m = 1$ and $n \ne m$

$$R^1_{n,m}(\psi_0) = \frac{1-\cos^2\psi_0}{(n-m)(n+m+1)} \left[P_{n,1}(\cos\psi_0)\frac{\mathrm{d}P_{m,1}(\cos\psi)}{\mathrm{d}\cos\psi} - P_{m,1}(\cos\psi_0)\frac{\mathrm{d}P_{n,1}(\cos\psi)}{\mathrm{d}\cos\psi}\right], \tag{A19}$$

and computed by the following recursive formula:

$$R^1_{n,n}(\psi_0) = \frac{n}{n-1}\frac{2n-1}{2n+1} R^1_{n+1,n-1}(\psi_0) + \frac{n+1}{n-1}\frac{2n-1}{2n+1} R^1_{n-1,n-1}(\psi_0) - \frac{n}{n-1} R^1_{n,n-2}(\psi_0), n > 1, \tag{A20}$$

The seed value for the recurrence is $R_{1,1}(\psi_0) = \frac{\cos^3\psi_0}{3} - \cos\psi_0 - \frac{2}{3}$.

Appendix C: Far-zone contributions for horizontal components

Molodensky-type truncation coefficients V^H_n defined in Eq. (27) are applied for evaluation of the far-zone contributions to the horizontal components of GDVs

$$\begin{bmatrix} \delta g_N^{FZ}(r,\Omega) \\ \delta g_E^{FZ}(r,\Omega) \end{bmatrix} = \frac{1}{4\pi R}\int_0^{\pi}\int_0^{2\pi} T(R,\alpha,\psi) \sum_{n=\ell+1}^{L} \frac{2n+1}{2n(n+1)} \mathrm{V}^H_n(R,\psi_0,r) P_{n,1}(\cos\psi) \begin{bmatrix} \cos\alpha \\ \sin\alpha \end{bmatrix} \sin\psi\;\mathrm{d}\alpha\mathrm{d}\psi. \tag{A21}$$

From $\frac{\partial P_n(\cos\psi)}{\partial\varphi} = \cos\alpha P_{n,1}(\cos\psi)$ and $\frac{1}{\cos\varphi}\frac{\partial P_n(\cos\psi)}{\partial\lambda} = \sin\alpha P_{n,1}(\cos\psi)$, we get

$$\begin{bmatrix} \delta g_N^{FZ}(r,\Omega) \\ \delta g_E^{FZ}(r,\Omega) \end{bmatrix} = \frac{1}{4\pi R}\sum_{n=0}^{L} \frac{2n+1}{2n(n+1)} V^H_n (R,\psi_0,r) \int_0^{\pi}\int_0^{2\pi} T(R,\alpha,\psi) \begin{bmatrix} \frac{\partial P_n(\cos\psi)}{\partial\varphi} \\ \frac{1}{\cos\varphi}\frac{\partial P_n(\cos\psi)}{\partial\lambda} \end{bmatrix} \sin\psi\;\mathrm{d}\alpha\mathrm{d}\psi. \tag{A22}$$

Considering definition of Laplace's surface harmonics T_n of the disturbing potential (Heiskanen and Moritz 1967, Sec. 2–14)

$$T_n(\Omega) = \frac{2n+1}{4\pi} \int_0^{\pi} \int_0^{2\pi} T(R,\alpha,\psi)\, P_n(\cos\psi)\, \sin\psi \,\mathrm{d}\alpha\, \mathrm{d}\psi, \tag{A23}$$

their differentiation with respect to φ, λ yields

$$\begin{bmatrix} \frac{\partial T_{\mathrm{n}}(\Omega)}{\partial\varphi} \\ \frac{1}{\cos\varphi}\frac{\partial T_n(\Omega)}{\partial\lambda} \end{bmatrix} = \frac{2n+1}{4\pi} \int_0^{\pi} \int_0^{2\pi} T(R,\alpha,\psi) \begin{bmatrix} \frac{\partial P_n(\cos\psi)}{\partial\varphi} \\ \frac{1}{\cos\varphi}\frac{\partial P_n(\cos\psi)}{\partial\lambda} \end{bmatrix} \sin\psi \,\mathrm{d}\alpha\, \mathrm{d}\psi. \tag{A24}$$

Using the derivatives in Eq. (A24), the far-zone contributions for the horizontal GDV components finally read

$$\begin{bmatrix} \delta g_N^{FZ}(r,\Omega) \\ \delta g_E^{FZ}(r,\Omega) \end{bmatrix} = \frac{GM}{2R^2} \sum\nolimits_{n=0}^{L} \frac{1}{n(n+1)} V_n^H(R,\psi_0,r) \begin{bmatrix} \frac{\partial T_{\mathrm{n}}(\Omega)}{\partial\varphi} \\ \frac{1}{\cos\varphi}\frac{\partial T_n(\Omega)}{\partial\lambda} \end{bmatrix}. \tag{A25}$$

Acknowledgements
Not applicable.

Author contributions

M.G. and I.F. designed the study, performed numerical analysis, and wrote the first draft of the paper. S.P. and S.F. contributed to the study design, and the data analysis, and reviewed/commented on the paper. P.N. reviewed the study design, numerical analysis, and the paper, and commented on all of them.

Funding
Ismael Foroughi was supported by Mitacs Application No. IT25135. Pavel Novák was supported by the project GA23-07031S of the Czech Science Foundation.

Data availability

The datasets generated and/or analyzed during the current study are available from the corresponding author upon reasonable request.

Declarations

Competing interests

The authors declare that they have no competing interests relevant to the content of this manuscript.

Author details
[1]Faculty of Civil Engineering, Shahrood University of Technology, Shahrood, Iran. [2]Department of Earth and Space Science and Engineering, York University, Toronto, Canada. [3]Sander Geophysics Ltd., Ottawa, Canada. [4]NTIS—New Technologies for the Information Society, Faculty of Applied Sciences, University of West Bohemia, Pilsen, Czech Republic. [5]Surveyor General Branch, Canadian Geodetic Survey, Natural Resources Canada, Ottawa, Canada.

Received: 27 May 2025 Accepted: 16 August 2025

References

Afrasteh Y, Safari A, Sheng M, Kingdon RW, Foroughi I (2019) The effect of noise on geoid height in Stokes-Helmert method. In: Vergos GS, Pail R, Barzaghi R (eds) International symposium on gravity, geoid and height systems 2016. Springer International Publishing, Berlin, pp 25–29. https://doi.org/10.1007/1345_2017_25

Ågren J, Sjöberg LE (2014) Investigation of gravity data requirements for a 5 mm-quasigeoid model over Sweden. In: Marti U (ed) Gravity, geoid and height systems. Springer International Publishing, Berlin, pp 143–150. https://doi.org/10.1007/978-3-319-10837-7_18

Argyle M, Ferguson S, Sander L, Sander S (2000) AIRgrav results: a comparison of airborne gravity data with GSC test site data. Lead Edge 19(10):1134–1138. https://doi.org/10.1190/1.1438494

Bayoud FA (2001) Some investigations on local geoid determination from airborne gravity data (MSc Thesis, Department of Geomatics Engineering, University of Calgary, Report No. 20154).https://prism.ucalgary.ca/bitstreams/f3f5952e-8c35-4fb7-8892-db771441fde3/download.

Becker D (2016) Advanced calibration methods for strapdown airborne gravimetry (PhD Thesis No. 51, Schriftenreihe der Fachrichtung Geodäsie, Technische Universität Darmstadt; oral defense: 1 September 2016, Darmstadt, Germany). https://tuprints.ulb.tu-darmstadt.de/5691/.

Bidel Y, Zahzam N, Bresson A, Blanchard C, Bonnin A, Bernard J, Cadoret M, Jensen TE, Forsberg R, Salaun C, Lucas S, Lequentrec-Lalancette MF, Rouxel D, Gabalda G, Seoane L, Vu DT, Bruinsma S, Bonvalot S (2023) Airborne absolute gravimetry with a quantum sensor, comparison with classical technologies. J Geophys Res Solid Earth 128(4):e2022JB025921. https://doi.org/10.1029/2022JB025921

Bolotin Y, Golovan A, Vyazmin V, Evstifeev M, Vershovskii A (2022) Advanced gravity field survey methods. In: Peshekhonov VG, Stepanov OA (eds) Methods and technologies for measuring the Earth's gravity field parameters. Springer International Publishing, Berlin, pp 237–301. https://doi.org/10.1007/978-3-031-11158-7_5

Chang G, Zhang X, Yu H (2024) Spherical radial basis functions model: approximating an integral functional of an isotropic Gaussian random field. J Geod 98:105. https://doi.org/10.1007/s00190-024-01910-w

Deng K, Chang G, Huang M, Zeng H, Chen X (2020) Geoid determination using band limited airborne horizontal gravimetric data. J Spat Sci. https://doi.org/10.1080/14498596.2020.1746703

Featherstone WE, McCubbine JC, Brown NJ, Claessens SJ, Filmer MS, Kirby JF (2018) The first Australian gravimetric quasigeoid model with location-specific uncertainty estimates. J Geod 92(2):149–168. https://doi.org/10.1007/s00190-017-1053-7

Feizi M, Raoofian-Naeeni M, Han S-C (2021) Comparison of spherical cap and rectangular harmonic analysis of airborne vector gravity data for high-resolution (1.5 km) local geopotential field models over Tanzania. Geophys J Int 227(3):1465–1479. https://doi.org/10.1093/gji/ggab280

Ferguson S, Wang Y, Ellief S, Li X, Holmes S, Ahlgren K, Xi R (2017) A comparison of airborne vector gravimeter measurements with the Geoid Slope Validation Survey 2014. IAG-IASPEI, Kobe

Foroughi I, Vaníček P, Kingdon RW, Goli M, Sheng M, Afrasteh Y, Novák P, Santos MC (2019) Sub-centimetre geoid. J Geod 93(6):849–868. https://doi.org/10.1007/s00190-018-1208-1

Foroughi I, Goli M, Pagiatakis S, Ferguson S, Novák P (2023) Data requirements for the determination of a sub-centimetre geoid. Earth-Sci Rev 239:104326. https://doi.org/10.1016/j.earscirev.2023.104326

Forsberg R, Olesen A, Bastos L, Gidskehaug A, Meyer U, Timmen L (2000) Airborne geoid determination. Earth Planets Space 52(10):863–866. https://doi.org/10.1186/BF03352296

Förste C, Bruinsma Sean L, Abrikosov O, Lemoine J-M, Marty JC, Flechtner F, Balmino G, Barthelmes F, Biancale R. EIGEN-6C4 The latest combined global gravity field model including GOCE data up to degree and order 2190 of GFZ Potsdam and GRGS Toulouse (p. 55102156 Bytes, 3 Files) [Application/octet-stream,application/octet-stream,application/zip]. GFZ Data Services. 2014. https://doi.org/10.5880/ICGEM.2015.1

Goli M, Foroughi I, Novák P (2018) On estimation of stopping criteria for iterative solutions of gravity downward continuation. Can J Earth Sci 55(4):397–405. https://doi.org/10.1139/cjes-2017-0208

Goli M, Foroughi I, Novák P (2019a) Application of the one-step integration method for determination of the regional gravimetric geoid. J Geod 93(9):1631–1644. https://doi.org/10.1007/s00190-019-01272-8

Goli M, Foroughi I, Novák P (2019b) The effect of the noise, spatial distribution, and interpolation of ground gravity data on uncertainties of estimated geoidal heights. Stud Geophys Geod 63(1):35–54. https://doi.org/10.1007/s11200-018-1013-6

Golovan AA, Vyazmin VS (2023) Methodology of airborne gravimetry surveying and strapdown gravimeter data processing. Gyrosc Navig 14(1):36–47. https://doi.org/10.1134/S2075108723010029

Heiskanen W A, Moritz H (1967) Physical Geodesy. San Francisco: W. H. Freeman & Co.; 364 pages. ISBN-10: 0716702339; ISBN-13: 978-0716702337.

Koch K-R, Kusche J (2002) Regularization of geopotential determination from satellite data by variance components. J Geodesy 76(5):259–268. https://doi.org/10.1007/s00190-002-0245-x

Krasnov A, Sokolov A, Bolotin Yu, Golovan A, Parusnikov N, Motorin A, Nosov A, Stepanov OA, Yurist S, Vyazmin V (2022) Data processing methods for onboard gravity anomaly measurements. In: Peshekhonov VG, Stepanov OA (eds) Methods and technologies for measuring the earth's gravity field parameters. Springer International Publishing, Berlin, pp 63–150. https://doi.org/10.1007/978-3-031-11158-7_2

Lacoste LJB (1967) Measurement of gravity at sea and in the air. Rev Geophys 5(4):477–526

Li X, Huang J, Klees R, Forsberg R, Willberg M, Slobbe DC, Hwang C, Pail R (2022) Characterization and stabilization of the downward continuation problem for airborne gravity data. J Geod 96(4):18. https://doi.org/10.1029/RG005i004p00477

Novák P (2003) Geoid determination using one-step integration. J Geod 77:193–206. https://doi.org/10.1007/s00190-003-0314-9

Novák P, Kern M, Schwarz K-P, Sideris MG, Heck B, Ferguson S, Hammada Y, Wei M (2003) On geoid determination from airborne gravity. J Geod 76(9):510–522. https://doi.org/10.1007/s00190-002-0284-3

Novák P, Šprlák M, Pitoňák M (2021) On determination of the geoid from measured gradients of the Earth's gravity field potential. Earth Sci Rev 221:103773. https://doi.org/10.1016/j.earscirev.2021.103773

Paige CC, Saunders MA (1982) LSQR: an algorithm for sparse linear equations and sparse least squares. ACM Trans Math Softw 8(1):43–71. https://doi.org/10.1145/355984.355989

Paul M (1973) A method of evaluating the truncation error coefficients for geoidal heights. Bull Geod 110:413–425. https://doi.org/10.1007/BF02521951

Rexer, M. (2017). Spectral solutions to the topographic potential in the context of high-resolution global gravity field modelling. PhD Thesis, Technical University of Munich. https://mediatum.ub.tum.de/1349781

Sander S, Argyle M, Elieff S, Ferguson S, Lavoie V, Sander L (2005) The AIRGrav airborne gravity system. CSEG RECORDER Magazine, 30(8) https://www.csegrecorder.com/articles/view/the-airgrav-airborne-gravity-system

Sander L, Ferguson S, Sander S (2011) Advances in SGL AIRGrav Acquisition and Processing. Paper presented at the ASEG-PESA Airborne Gravity 2010 Workshop, published in Geoscience Australia Record 2010/23 (2011). https://www.semanticscholar.org/paper/Advances-in-SGL-AIRGrav-Acquisition-and-Processing-SanderFerguson/942505891499f80fcb3c2c8688842c9070c50beb#citing-papers

Schwarz K-P, Li YC (1996) What can airborne gravimetry contribute to geoid determination? J Geophys Res Solid Earth 101(B8):17873–17881. https://doi.org/10.1029/96JB00819

Schwarz KP, Kern M, Nassar SM (2002) Estimating the gravity disturbance vector from airborne gravimetry. In: Ádám J, Schwarz K-P (eds) Vistas for geodesy in the New Millennium. Springer, Berlin, pp 199–204. https://doi.org/10.1007/978-3-662-04709-5_33

Semernya EI, Skobelev SP (2019) On evaluation of indefinite integrals containing products of associated Legendre functions. J Phys: Conf Ser 1352(1):012046. https://doi.org/10.1088/1742-6596/1352/1/012046

Serpas JG, Jekeli C (2005) Local geoid determination from airborne vector gravimetry. J Geod 78(10):577–587. https://doi.org/10.1007/s00190-004-0416-z

Swain CJ (1996) Horizontal acceleration corrections in airborne gravimetry. Geophysics 61(1):273–276. https://doi.org/10.1190/1.1443948

Vajda P, Foroughi I, Vaníček P, Kingdon R, Santos M, Sheng M, Goli M (2020) Topographic gravimetric effects in earth sciences: review of origin, significance and implications. Earth-Sci Rev. https://doi.org/10.1016/j.earscirev.2020.103428

Vaníček Vaníček P, Huang J, Novák P, Pagiatakis S, Veronneau M, Martinec Z, Featherstone W (1999) Determination of the boundary values for the Stokes-Helmert problem. J Geod. https://doi.org/10.1007/s001900050235

Vaníček P, Kleusberg A (1987) Canadian geoid: stokesian approach. Manuscr Geodaet 12:86–98. https://doi.org/10.1007/BF03655117

Vaníček P, Tenzer R, Sjöberg LE, Martinec Z, Featherstone WE (2004) New views of the spherical Bouguer gravity anomaly. Geophys J Int 159(2):460–472. https://doi.org/10.1111/j.1365-246X.2004.02435.x

Vyazmin VS (2023) New algorithm for gravity vector estimation from airborne data using spherical scaling functions. In JT Freymueller, L Sánchez (Eds). 5th Symposium on Terrestrial Gravimetry: Static and Mobile Measurements (TG-SMM 2019). Springer International Publishing. 51–57. https://doi.org/10.1007/1345_2020_113

Vyazmin V, Golovan A (2023a) IMU and GNSS postprocessing for high-resolution strapdown airborne gravimetry. Eng Proc 54(1):Article 1. https://doi.org/10.3390/ENC2023-15455

Vyazmin V, Golovan A (2023b) Scalar and vector strapdown airborne gravimetry on aircraft and UAV: methodology of surveying and data processing. 2023 30th Saint Petersburg International Conference on Integrated Navigation Systems (ICINS), 1–6. https://doi.org/10.23919/ICINS51816.2023.10168453

Vyazmin V, Golovan A, Bolotin Y (2021) New Strapdown airborne gravimetry algorithms: testing with real flight data. 2021 28th Saint Petersburg International Conference on Integrated Navigation Systems (ICINS), 1–7. https://doi.org/10.23919/ICINS43216.2021.9470826

Wang YM, Becker C, Mader G, Martin D, Li X, Jiang T, Breidenbach S, Geoghegan C, Winester D, Guillaume S, Bürki B (2017) The geoid slope validation survey 2014 and GRAV-D airborne gravity enhanced geoid comparison results in Iowa. J Geod 91(10):1261–1276. https://doi.org/10.1007/s00190-017-1022-1

Wang YM, Sánchez L, Ågren J, Huang J, Forsberg R, Abd-Elmotaal HA, Ahlgren K, Barzaghi R, Bašić T, Carrion D, Claessens S, Erol B, Erol S, Filmer M, Grigoriadis VN, Isik MS, Jiang T, Koç Ö, Krcmaric J, Li X, Liu Q, Matsuo K, Natsiopoulos DA, Novák P, Pail R, Pitoňák M, Schmidt M, Varga M, Vergos GS, Véronneau M, Willberg M, Zingerle P (2021) Colorado geoid computation experiment: overview and summary. J Geod 95(12):127. https://doi.org/10.1007/s00190-021-01567-9

Willberg M, Zingerle P, Pail R (2020) Integration of airborne gravimetry data filtering into residual least-squares collocation: example from the 1 cm geoid experiment. J Geodesy 94(8):75. https://doi.org/10.1007/s00190-020-01396-2

Xu P, Shen Y, Fukuda Y, Liu Y (2006) Variance component estimation in linear inverse Ill-posed models. J Geodesy 80(2):69–81. https://doi.org/10.1007/s00190-006-0032-1Geodesy

Zhao Q, Xu X, Forsberg R, Strykowski G (2018) Improvement of downward continuation values of airborne gravity data in Taiwan. Remote Sens 10(12):Article 12. https://doi.org/10.3390/rs10121951

Zhong D, Damiani TM, Preaux SAM, Kingdon RW (2015) Comparison of airborne gravity processing results by GravPRO and Newton software packages. Geophysics 80(4):G107–G118. https://doi.org/10.1190/geo2014-0519.1

Zingerle P, Pail R, Gruber T, Oikonomidou X (2020) The combined global gravity field model XGM2019e. J Geod 94(7):66. https://doi.org/10.1007/s00190-020-01398-0

Li X (2011) Strapdown INS/DGPS airborne gravimetry tests in the Gulf of Mexico. Journal of Geodesy, 85(9), 597–605. https://doi.org/10.1007/s00190-011-0462-2

Jekeli C, Kwon JH (2002) Geoid profile determination by direct integration of GPS inertial navigation system vector gravimetry. Journal of Geophysical Research: Solid Earth, 107(B10), ETG 3-1 – ETG 3-10. https://doi.org/10.1029/2001JB001626

Liu X, Li Y, Xiao Y, Guan B (2015) Downward continuation of airborne geomagnetic data based on two iterative regularization methods in the frequency domain. Geodesy and Geodynamics, 6(1), 34–40. https://doi.org/10.1016/j.geog.2014.12.003

Strykowski G, Forsberg R (1998) Operational merging of satellite, airborne and surface gravity data by draping techniques. In: R. Forsberg, C. Feissel R. Dietrich (eds.), Geodesy on the Move: Gravity, Geoid, Geodynamics and Antarctica (Proceedings of the IAG Scientific Assembly, Rio de Janeiro, Sept. 3–9, 1997). International Association of Geodesy Symposia, Vol. 119, pp. 243–248. Springer, Berlin, Heidelberg.

Publisher's Note